Selective synthesis of α, β, and γ-Ag_2WO_4 polymorphs: promising platforms for photocatalytic and antibacterial materials

Roman Alvarez-Roca[1], Amanda Fernandes Gouveia[2,3], Camila Cristina de Foggi[1], Pablo Santana Lemos[1], Lourdes Gracia[3,a)], Luís Fernando da Silva[4], Carlos Eduardo Vergani[5], Miguel San-Miguel[2], Elson Longo[1], Juan Andrés[3]*

[1]CDMF, Federal University of São Carlos, P.O. Box 676, 13565-905, São Carlos, SP, Brazil
[2]Institute of Chemistry, State University of Campinas, Unicamp, 13083-970, Campinas, SP, Brazil
[3]Dept. of Química Física i Analítica, Universitat Jaume I, 12071 Castelló de la Plana, Spain
[4]Physics Dept., Federal University of São Carlos, P.O. Box 676, 13565-905, São Carlos, SP, Brazil
[5]São Paulo State University (Unesp), P.O. Box 1680, 14801903, Araraquara, SP, Brazil.
[a)]Permanent address: Physical Chemistry Dept., Universitat de Valencia, 46100 Burjassot, Spain

* corresponding author: andres@qfa.uji.es

ABSTRACT

Silver tungstate (Ag_2WO_4) shows structural polymorphism with different crystalline phases, namely orthorhombic, hexagonal, and cubic structures that are commonly known as α, β, and γ, respectively. In this work, these Ag_2WO_4 polymorphs were selectively and successfully synthesized through a simple precipitation route at ambient temperature. The polymorph-controlled synthesis was conducted by means of the volumetric ratios of the silver nitrate/tungstate sodium dehydrate precursors in solution. The structural and electronic properties of the as-synthetized Ag_2WO_4 polymorphs were investigated by using a combination of X-ray diffraction and Rietveld refinements, X-ray absorption spectroscopies, X-ray absorption near edge structure spectroscopy, field emission-scanning electron microscopy images, and photoluminescence. To complement and rationalize the experimental results, first-principles calculations, at density functional theory level, were carried out, leading to an unprecedented glimpse into the atomic-level properties of the morphology and the exposed surfaces of Ag_2WO_4 polymorphs. Following the analysis of the local coordination of Ag and W cations (clusters) at each exposed surface of the three polymorphs, the structure–property relationship between the morphology and the photocatalytic and antibacterial activities against Amiloride degradation under ultraviolet light irradiation and methicillin-resistant *Staphylococcus aureus*, respectively, was investigated. A possible mechanism of the photocatalytic and antibacterial activity as well the formation process and growth of the polymorphs is also explored and proposed.

Keywords: Silver tungstate, α-, β- and γ-polymorphs, synthesis, photocatalysis, antibacterial, morphology.

INTRODUCTION

Polymorphism is the ability of a chemical system to adopt different crystallized structures with identical chemical composition but different stabilities. As the crystal structure determines the properties of a material, polymorphism can have a direct impact on its functional properties, and thus on its technological applications. Different polymorphs can have dramatically different chemical, physical, and biological properties. Often these changes in their crystal structure can lead to novel properties and the opening up of potential applications in several research areas, like photocatalysts, sensing gas, ion conductors, among others.[1,2,3,4,5,6,7,8,9,10]

Polymorphs of binary or complex metal oxides are well known in several oxides, namely TiO_2, $CaCO_3$, ZrO_2, WO_3, as well as zeolites and SiO_2, etc.[11,12,13,14,15,16] These polymorphs have different stabilities and may transform, under particular conditions, from an unstable form (metastable phase) to a more stable polymorph. Metastable polymorphs are relevant for science and technology, offering more promising new design opportunities (both experimental and theoretical) to obtain superior properties for some applications than their corresponding stable phase.[17,18,19,20,21,22,23] Due to difficulties in its control, polymorphism has been often considered a drawback in technological applications, limiting the development of various multifunctional materials. Therefore, the understanding of the relationship between crystal structure and its functional properties is essential for a rational design of the synthesis, property and function of polymorphism.[24] Recently, Gentili et al.[10] published a review highlighting representative progress in the control and applications of polymorphism as an additional functionality of materials for technological applications.

Solid-state synthesis methods typically rely on equilibrium routes in which the most stable polymorph is obtained, whereas the metastable solid polymorphs tend to form *via*

non-equilibrium or metastable states,[25,24,26] that may be attained upon quenching an intermediate of the reaction or by different synthetic methods, such as gas phase, hydrothermal, mechanochemical or template synthesis.[27] The polymorph-controlled synthesis of inorganic compounds, though crucially important, still remains a great challenge, offering remarkable opportunity for discovering multifunctional materials with unusual properties.[28] While it is well established that the kinetics required to form different polymorphs from a specific precursor can often be manipulated by changing their synthesis conditions to obtain a metastable phase, the relative stability of kinetically accessible phases often fall within a fairly narrow range of energies. Yet, the fundamental understanding of which metastable phases can be synthesized, and whether or not synthesizability is related to the excess enthalpy of a metastable phase above its thermodynamic ground state, is still lacking.[19,21] Answering this would enable a more rational approach in order to design and synthesize of inorganic metastable phases and desirably assist in their experimental realization.[29,30]

Silver tungstate (Ag_2WO_4) has received considerable attention in recent years due to its attractive characteristics, applicable in a wide range of practical scenarios. Ag_2WO_4 is a wide-band gap multifunctional semiconductor material that presents structural polymorphism and can crystallize in three different structures. Among them, the α phase is, thermodynamically, the most stable one.[31,32,33] In addition to α-polymorph, with orthorhombic structure and space group ($Pn2n$), the β- and γ-metastable, with hexagonal structure and space group ($P6_3/m$) and cubic and space group ($Fd\bar{3}m$), respectively, have also been described. α-Ag_2WO_4 presents unique structural properties[34] with a wide range of electrical and optical properties that can offer widespread applications ranging from

photocatalysis, gas sensor, antibacterial and antifungal agents, and photoluminescence (PL) emissions, among others.[32,34,35,36,37,38,39,40,41,42,43,44,45,46, 47,48,49]

Ag_2WO_4 polymorphs have been synthesized by different methods, such as: precipitation,[31,37,50,51,52,53] conventional hydrothermal,[37,54] microwave-assisted hydrothermal,[34,37, 38, 55,56,57] sonochemical,[37,41,58,59] and simple ion exchange.[60] Recently, controlled precipitation was reported in the preparation of metastable β-Ag_2WO_4[52] where the Eu ions addition was used as a stabilizer agent of the metastable β-phase. Similarly, through a facile precipitation process in the presence of surfactants acting as a phase stabilizer, other authors have also reported the obtainment of this polymorph.[56,61,62] The preparation of β-Ag_2WO_4 through a conventional precipitation route, without any assisted procedure, has also been reported.[43,63,64,65] Yet, to date, the preparation of metastable γ-Ag_2WO_4 has been scarcely reported. For example, this polymorph was obtained through a simple controlled precipitation method at room temperature[66] and by surfactant-assisted.[67] However, these synthesis processes are frequently unselective because they involve the production of a mixture of the different polymorphs and also affect their dimension, morphology, microstructure, and subsequent functionality significantly. Different synthesis conditions yield different polymorphs and highlight the complexity of the energy landscape during the crystal formation process.

From a scientific point of view, our interest is to provide novel and selective routes to synthesize α-, β- and γ-Ag_2WO_4 polymorphs separately. Thus, this study presents an experimental and theoretical investigation of the Ag_2WO_4 polymorphs, which were selectively synthesized from two common precursors thanks to the careful control of the synthesis conditions which, in turn, revealed an alternative way to control Ag_2WO_4´s polymorphism. Establishing the atomic-scale structure of the surfaces is a key step to model

this kind of materials. Guided by the density functional theory (DFT) findings, we will disclose the delicate morphology and defect control of its antibacterial and photocatalytic mechanisms, to comprehend, predict, and explain how these emerge. Finally, a number of insights on the role of the local coordination of the Ag and W cations, in the three polymorphs, together with the crystallization process as a function of solution chemistry will be provided, allowing us to propose a mechanism for the nucleation and growth processes by using the concept of clusters, namely $[AgO_x]$ and $[WO_y]$, as building blocks of the different α-, β-, and γ-phases.

The structures and electronic properties of the as-synthesized samples were studied through X-ray diffraction (XRD) with Rietveld refinements, X-ray photoelectron spectroscopies (XPS), and X-ray absorption near-edge spectroscopy (XANES). Their optical properties were studied by using PL emissions. Field emission-scanning electron microscopy (FE-SEM) images were employed to analyze their morphological evolution. The performance of the as-synthetized polymorphs as antibacterial agents against methicillin-resistant *Staphylococcus aureus* (MRSA) and their photocatalytic degradation of amiloride (AML) under ultraviolet (UV) light irradiation were also studied. First-principles calculations, based on DFT, were performed to calculate the relative energy between different phases, their electronic structures, as well as their surface energies. We applied a joint experimental and theoretical strategy, which we developed ourselves, to rationalize the experimental morphologies of the α-, β- and γ-Ag_2WO_4 polymorphs.

The article is organized as follows. In Section 2, the experimental methods are presented. This section comprises four subsections: the synthetic procedure, the characterization techniques, the antibacterial and photocatalytic activities, and the

computational methods and model systems. Section 3 presents the results and the discussion. The main conclusions are summarized in the last section, Section 4

EXPERIMENTAL SECTION

Synthesis procedure

The three different polymorphs of Ag_2WO_4 were synthesized via a simple precipitation method at 25ºC under constant stirring during 10 min without any surfactant, as previously reported in our previous works [34,66,68]. Tungstate sodium dihydrate ($Na_2WO_4{\cdot}2H_2O$; 99.5% purity, Sigma-Aldrich) and silver nitrate ($AgNO_3$; 99.8% purity, Sigma-Aldrich) were used as precursors salts as received. In a typical synthesis procedure of Ag_2WO_4 crystals, appropriate quantities of $AgNO_3$ and $Na_2WO_4{\cdot}2H_2O$ were dissolved separately into 50 mL of de ionized water. After 5 min of stirring, to ensure complete dissolution, the $AgNO_3$ solution was then added to the $Na_2WO_4{\cdot}2H_2O$ solution under continuous stirring. The resulting suspensions were collected using centrifugation methods. They were washed several times using acetone to remove the remaining ions and then dried in an oven at room temperature for 6 h. The chosen ratio for the precursor concentrations was 2:1, $AgNO_3$:$Na_2WO_4{\cdot}2H_2O$. The concentration values between 0.0035 M to 0.33 M were explored to find the most appropriate combination for the selective synthesis of the three polymorphs.

Characterization techniques

In order to confirm the crystalline phase and purity of the polymorphs, their XRD patterns were obtained and indexed according to the reported patterns of each polymorph. The crystals were characterized using an X-ray diffractometer, model LabX XRD-6000

(Shimadzus, Japan) with Cu-Kα irradiation source (λ=0.15418nm) at a scan rate (2θ) of $0.05°s^{-1}$, in a range from 5° to 120°. Their size and shapes were examined using a FE-SEM Inspect F50 (FEI Company, Hillsboro, OR) operated at different magnifications. XANES measurements were performed at the XAFS2 beamline at the Brazilian Synchrotron Light Laboratory (LNLS). XANES spectra were collected at W L1 edges in a transmission mode at room temperature (using energy steps of 1.0 eV). For the XANES spectra analysis, the background was removed from all the spectra, which were then normalized by first extended X-ray absorption fine structure (EXAFS) oscillation using MAX software [69].

PL emissions spectra were measured at room temperature by using a Monospec 27 monochromator (Thermal, Jarrel Ash, USA) coupled to a Hamamatsu Photonics R446 photomultiplier (Japan). A krypton ion laser (Coherent Innova, 200 K, USA) was used as excitation source (k = 350 nm). The incident laser beam power on the sample was maintained at 15 mW. To chemical environment investigations, X-ray photoelectron spectroscopy (XPS) measurements were performed on a commercial Scientia Omicron ESCA (Germany) spectrometer using the monochromatic Al Kα line (1486.7 eV). Normalization was performed using a nonlinear Shirley's method. For the binding energy calibration of the elements, the peak of C1s element at 248.6 eV was used as reference.

Photocatalytic measurements

The photocatalytic activity was analyzed throughout the degradation process of Amiloride (AML) under UV light irradiation (in a photoreaction box with six Philips lamps, 15W, at 254 nm of maximum emission and 39 $mWcm^{-2}$ of optical irradiance). The photocatalytic degradation tests in the presence of Ag_2WO_4 polymorphs were conducted on 50 mg of each photocatalyst placed in contact with 50 mL of aqueous amiloride solution of

10 mgL^{-1} (10 ppm). Prior to the photodegradation experiments, the mixture of AML and the photocatalysts was kept in the dark for 2 h, under magnetic stirring, to ensure the adsorption–desorption equilibrium. No prominent adsorption effect of Ag_2WO_4 polymorphs on drug has been observed after 30 min of observation which established negligible absorption effects. The color removal of the dye solutions was monitored by measuring its UV–Vis spectra (JASCO V-660 spectrophotometer, λ_{max}= 362 nm for AML drug solution) at different times of light exposure. The experiments were performed in triplicate.

The Langmuir–Hinshelwood model was applied to assess the kinetic of a photocatalytic process, which is well described by the following equations:

$$r=dC/dt= kKC/(1 + KC) \quad (1)$$

When the concentration is low (1 >> KC) the above equation can be simplified to a pseudo first-order equation:

$$r=dC/dt= kKC \text{ and } \ln (C/C_o) = - kKt = k_{app}t \quad (2)$$

where r is the reaction rate, K is the adsorption coefficient, C_0 and C are the initial and residual concentration of AML, respectively, and k is the specific rate constant of the photoreaction. The photocatalytic degradation efficiency (PDE) was calculated according to the following equation:

$$PDE (\%) = (C/C_o)\times 100 \quad (3)$$

In order to detect the active species formed in this photocatalytic process, the so-called reactive oxygen species (ROS), a quencher experiment was performed by adding ascorbic acid (AA), isopropyl alcohol (IPA), and ammonium oxalate (AO), scavengers of the superoxide radical (O_2'), hydroxyl radical (OH^*) and hole ($h^\bullet$), respectively.

Antibacterial activity test

In this study, a standard methicillin-resistant *Staphylococcus aureus* (MRSA) strain obtained from the American Type Culture Collection (ATCC 33591), gram-positive bacteria, was used in the antibacterial experiments. The protocol for determining the minimum inhibitory and bactericidal concentrations (MIC and MBC, respectively) was performed following the procedure previously described elsewhere[70].

In order to better understand the bactericide activity of the Ag_2WO_4 polymorphs, a detailed analysis was performed in FE-SEM and confocal laser scanning microscopy (CLSM). The microorganisms were exposed to the respective sub-inhibitory concentration of each material in a 24-well plate and were later on incubated in a static oven during 24 h. For FE-SEM analysis, the samples were washed with phosphate buffered saline (PBS), submerged in 5% paraformaldehyde for 1 h, washed twice with PBS, and dissected with ethanol in increasing concentrations (70%, 80% and 90% for 5 min). The finishing was done with 100% alcohol in three washes of 5 min each. Afterwards, the samples were mounted on metal stubs and held in *vacuum* dissectors until the analysis.

For the monitoring of viability of the bacteria by confocal microscope, the cells submitted to treatment were washed twice with PBS, and labeled with the LIVE/DEAD BacLight Kit, at 25ºC, following to the manufacturer's recommendations. The analyses were performed under a microscope Carl Zeiss LSM 800. The images were analyzed in ZEN BLUE 2.3 System.

Computational methods and model systems

In order to delve into the relationship of the structure and morphology of the α-, β- and γ-Ag_2WO_4 polymorphs, theoretical calculations were performed using the DFT associated

to the Perdew–Burke–Ernzerhof (PBE) formulation for the electron exchange and correlation contribution to the total energy[71,72] in the VASP program[73,74]. The electron–ion interaction was described through projector-augmented-wave pseudopotentials. The plane-wave expansion was truncated at a cut-off energy of 460 eV, and the Brillouin zones were sampled through the Monkhorst–Pack special k-point grid to ensure geometrical and energetic convergence for the Ag_2WO_4 crystal surfaces. Details of the slab thickness of the different surface models for the α-, β- and γ-Ag_2WO_4 polymorphs can be found in previous studies [34,66,68].

The band gap energy values and density of states (DOS) were obtained for both bulk and surfaces of Ag_2WO_4. To analyze the different kinds of Ag and W clusters at the exposed surfaces of each polymorph, a representation of the corresponding structure was performed by using the VESTA program[75].

The clean surfaces of each polymorph were simulated as follows: for the α-Ag_2WO_4 the (010), (001) and (101) surfaces have been selected. For β-Ag_2WO_4 and γ-Ag_2WO_4, the (011) and (110) surfaces, and (100), (101) and (111) surfaces have been investigated, respectively. The corresponding values of the surface energies (E^i_{surf}) were calculated by the equation (4):

$$E^i_{surf} = (E^i_{slab} - nE_{bulk})/2A \quad (4)$$

where E^i_{slab} is the total energy of the corresponding slab (i), n is the number of molecular units present in the slab, E_{bulk} is the energy of the bulk of each polymorph and $2A$ corresponding to the area of both sides of the slab. Calculating the E^i_{surf} values, and using the Wulff construction, results in a polyhedron that depends only on the ratios between the values of the surface energies and symmetry point group [76,77].

By combining simulations based on first-principles calculations at the DFT level with experimental studies, our research group has recently proved that this strategy is a valuable design aid to achieve an optimum morphology, since it offers a high-fidelity approach that results in rapid *in silico* prediction crystal growth habits. In addition, it allows us to establish a correlation between morphology, properties, and subsequent applications for both micro- and nanomaterials, such as ZnO[78], Ag_2O[79], Ag_3PO_4[80,81], α-Ag_2WO_4 [34,53], $PbMoO_4$[82], $BaWO_4$[83], and $ZnWO_4$[84,85]. A proof-of-concept has been developed, which demonstrates the automation feasibility of the models[86],[87],[88] to obtain the set of morphologies available and match the theoretical morphology with the images displayed by FE-SEM. This proof-of-concept also motivates their continued development.

The polyhedron energy $(E_{polyhedron})$ value of both morphologies (theoretical and experimental) according to methodology proposed by our research group[53] was also calculated. In this study, we went further and calculated the polyhedron band gap energy value ($E_{gap}^{polyhedron}$) for the α-, β- and γ-Ag_2WO_4 polymorphism, as follows:

$$E_{gap}^{polyhedron} = \sum_i C_i \times E_{gap}^{i} \quad (5)$$

where $C_i = A^i/A^{polyhedron}$, is the ratio of the surface area (A^i) to the total surface area of the polyhedron ($A^{polyhedron}$), and the E_{gap}^{i} is the band gap energy value of the corresponding surface (i).

RESULTS AND DISSCUSION

Structural characterization

Figure 1 (a-c) shows the XRD patterns of the samples with different ratios between the $AgNO_3$ and $Na_2WO_4{\cdot}2H_2O$ precursors. The pattern in Figure 1a is indexed with the cubic γ-

Ag_2WO_4 structure, in good agreement with the database (JCPDS 861157). A precursor concentration ratio of $AgNO_3$:$Na_2WO_4{\cdot}2H_2O$ equal to 0.33M:0.165M was used to obtain this polymorph. The intense and well-defined peaks indicate good crystallinity. By decreasing the concentration of the precursor salts until a molar concentration of 0.04M of $AgNO_3$ and 0.02M of $Na_2WO_4{\cdot}2H_2O$, the XRD peaks of the γ-Ag_2WO_4 disappeared and new peaks were identified. The new peaks were matched to the reflections of the hexagonal β-Ag_2WO_4 structure (JCPDS No. 331195), as shown in Figure 1b, in good accordance with our previous study[63]. Further decreasing the precursor's molar concentration until 0.007M and 0.0035M for $AgNO_3$ and $Na_2WO_4{\cdot}2H_2O$, respectively, a new XRD pattern was reached. The position and intensity of the well-defined XRD patter peaks, as displayed in Figure 1c, were indexed to the standard orthorhombic α-Ag_2WO_4 structure (JCPDS No. 34-0061). No peaks related to any secondary phase were identified indicating the formation of a pristine phase.

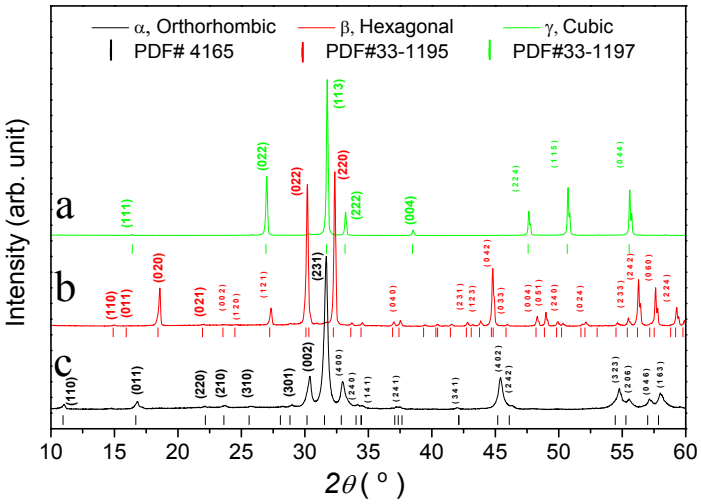

Figure 1. XRD patterns of the γ- (a), β- (b), and α-Ag_2WO_4 (c) polymorphs synthesized at stoichiometric precursor ratio of 2:1 and different precursors concentration.

Figure 2 presents the 3D structures of the α-, β- and γ-Ag_2WO_4 polymorphs, at the DFT level, following the optimized values of the geometry. An analysis of the results shows that Ag_2WO_4 polymorphs have a complicated network structure with a remarkable crystallographic inhomogeneity with an intrinsic anisotropy associated to their building blocks, i.e., the constituents $[AgO_x]$ and $[WO_y]$ clusters.

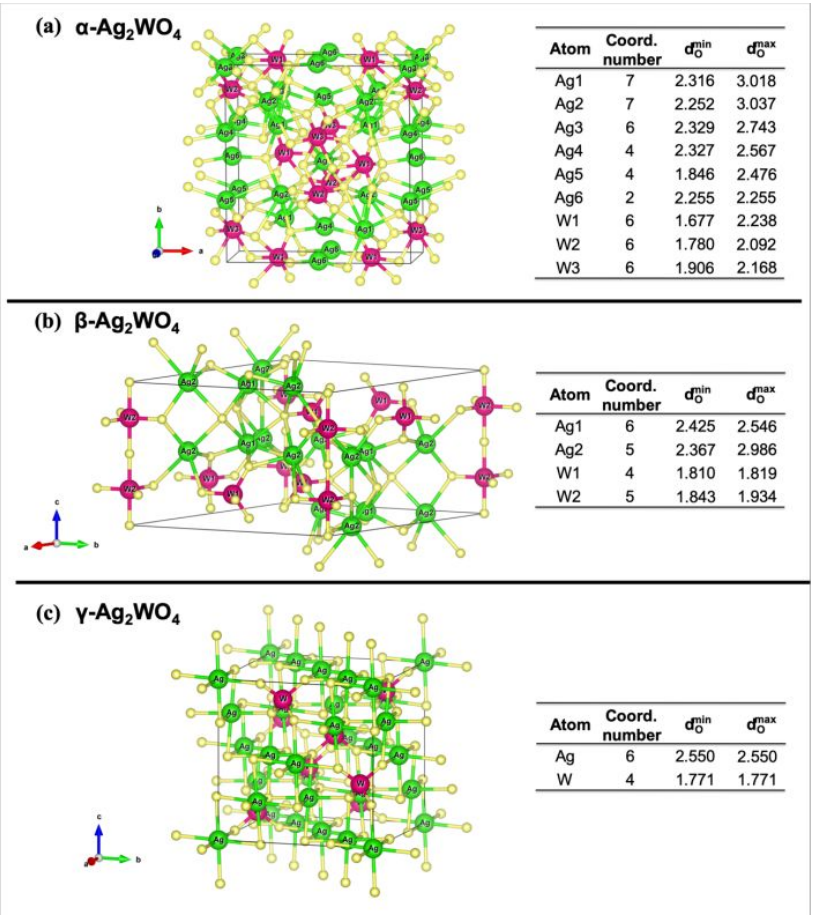

Atom	Coord. number	d_O^{min}	d_O^{max}
Ag1	7	2.316	3.018
Ag2	7	2.252	3.037
Ag3	6	2.329	2.743
Ag4	4	2.327	2.567
Ag5	4	1.846	2.476
Ag6	2	2.255	2.255
W1	6	1.677	2.238
W2	6	1.780	2.092
W3	6	1.906	2.168

Atom	Coord. number	d_O^{min}	d_O^{max}
Ag1	6	2.425	2.546
Ag2	5	2.367	2.986
W1	4	1.810	1.819
W2	5	1.843	1.934

Atom	Coord. number	d_O^{min}	d_O^{max}
Ag	6	2.550	2.550
W	4	1.771	1.771

Figure 2. Unit cell representation of (a) α-Ag_2WO_4, (b) β-Ag_2WO_4 and (c) γ-Ag_2WO_4 structures and Ag–O and W–O bond distances (minimum and maximum).

W cations shows different $[WO_y]$ (y = 4, 5 and 6) clusters, while Ag cations can display different $[AgO_x]$ type-coordination numbers, $[AgO_x]$ (x = 2, 4, 5, 6, and 7) clusters. The

piling up of these clusters builds the 3D structures of the different polymorphs. In the lattice of α-Ag_2WO_4, each W cation is bonded to six oxygens, forming three different distorted [WO_6] clusters with values of the W–O bond lengths in the range of 1.677-2.238 Å. The Ag cations are found to have [AgO_2] clusters with an Ag–O bond distance of 2.255 Å, two [AgO_4] clusters with Ag–O bond distances in the range 1.846-2.567 Å, an [AgO_6] cluster with Ag–O bond distances in the range of 2.329-2.743 Å, and two kind of [AgO_7] clusters with Ag–O bond distances in the range of 2.252 and 3.037 Å. Overall, there are four different distorted [AgO_x] (x = 2, 4, 6, and 7) clusters. The geometry of β-Ag_2WO_4 presents tetrahedral distorted [WO_4] clusters and trigonal bipyramidal distorted [WO_5] clusters and two types of distorted [AgO_x] (x= 5, and 6) clusters. Finally, the γ-Ag_2WO_4 polymorph is constituted by only [WO_4] and [AgO_6] symmetric clusters.

The nature of the structural deviations from ideal orthorhombic and hexagonal symmetries that alter key structural features like the Ag–O and W–O bond distances strongly influences their oxide electronic structure through 3*d* orbital occupancy and metal–oxygen orbital overlap. These electronic structure effects follow the elongation and compression of the metal–oxygen bond distances of the different clusters. The modification of the electronic bandwidth by the structural effects of strain alters a number of electronic features, like the metal *d*-band and O 2*p*-band centers. This has several implications in the electronic properties and a broad range of chemical properties.

XANES is a useful technique that enables the investigation of the local order structure of different materials, providing qualitative information on the absorber atom environment such as symmetry and oxidation state [37,89,90]. Figure 3 presents the W LI-edge XANES spectra of the Na_2WO_4 and WO_3 reference compounds and the as-prepared Ag_2WO_4

polymorphs (α, β, and γ phases). As can be observed, the environment around the W atoms is quite different for as-synthesized Ag_2WO_4 samples, indicating that the environment around W atoms is distinct for the samples. Figure 3a shows that the spectra of β- and γ-Ag_2WO_4 samples and the Na_2WO_4 reference present an intense pre-peak (labeled as A) at around 12.1 keV, while the α-Ag_2WO_4 and γ-WO_3 spectra exhibit a shoulder. According to literature, the physical origin of peak A is related to forbidden electron transitions from 2*s* →5*d* orbitals[91]. Yamazoe et al. reported that a less symmetric structure enhances the intense pre-peak because this forbidden electron transition is allowed by mixing the p orbitals of W atoms and the ligand into empty *d* orbitals[91]. The presence of an intense pre-peak in the W-L1 edge XANES spectrum has been reported in the compounds where the W atoms are coordinated by four oxygen atoms, such as Na_2WO_4, $Sc_2W_3O_{12}$ [91,92,93]. On the other hand, this pre-peak becomes less pronounced in the compounds where the W atoms are in a distorted octahedral configuration, for example the γ-WO_3 compound[91,92,93].

A detailed view of the pre-edge region, as depicted in Figure 3b, revealed that the γ-Ag_2WO_4 spectrum pre-edge region is quite similar to the Na_2WO_4 reference, indicating that γ-Ag_2WO_4 exhibits a tetrahedral configuration, i.e., [WO_4] clusters. In the case of the α-Ag_2WO_4 spectrum, it was similar to the γ-WO_3 spectrum, which suggests octahedral coordination, i.e., [WO_6] clusters. Regarding the β-phase spectrum, a slight reduction in the pre-peak intensity and an energy shift towards high values can be seen when compared to the Na_2WO_4 spectrum. These findings can be linked to the presence of [WO_5] clusters in the β-Ag_2WO_4 sample.

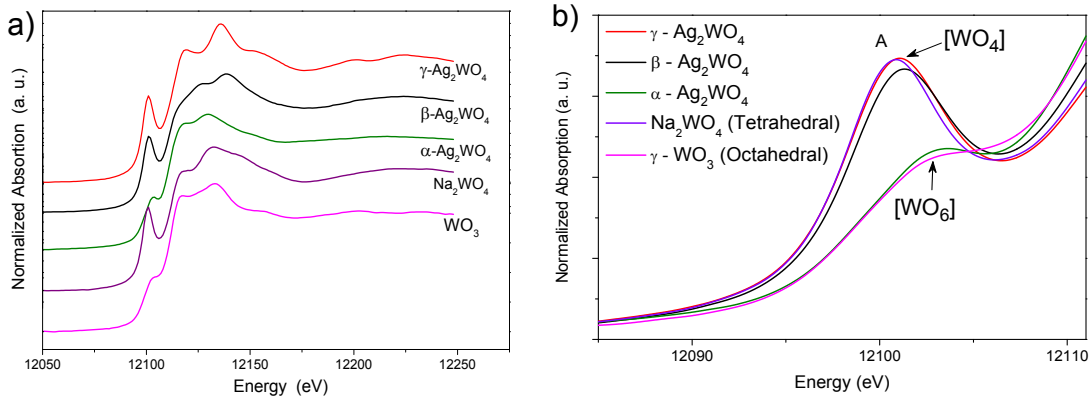

Figure 3. (a) Normalized W-L1 edge XANES spectra of references γ-WO_3, Na_2WO_4 and of Ag_2WO_4 samples presenting distinct crystalline phases (α-, β-, and γ-). (b) Detailed region of XANES pre-edge region displayed in (a).

Photocatalytic Activity

Figure 4a shows the photocatalytic activity of Ag_2WO_4 toward AML degradation under UV irradiation as a function of time. The different profiles of (C_0/C) versus *t* are shown for each Ag_2WO_4 polymorph. The results show that photolysis in the absence of catalysts was around 37% after 40 min of exposure. An analysis of the results shows that 92% of AML was photodegraded by α-Ag_2WO_4 at 40 min, while only 70% was degraded in the case of γ-Ag_2WO_4 at the same time under UV irradiation. When β-Ag_2WO_4 was the catalyst used, photodegradation was practically completed within just 30 min under UV irradiation. Overall, the AML photodegradation process with Ag_2WO_4 polymorphs exhibited better photocatalytic activities than without them, implying an efficient use of all Ag_2WO_4 polymorphs for AML environmental remediation. The pseudo-first-order kinetic equation, expressed as $\ln(C_0/C) = k_{app}t$, is shown in Figure 4b. As can be observed, the relation between $\ln(C_0/C)$ versus *t* has a fairly good correlation to the pseudo-first-order model, which indicates that AML degradation can be described well by this kinetic model.

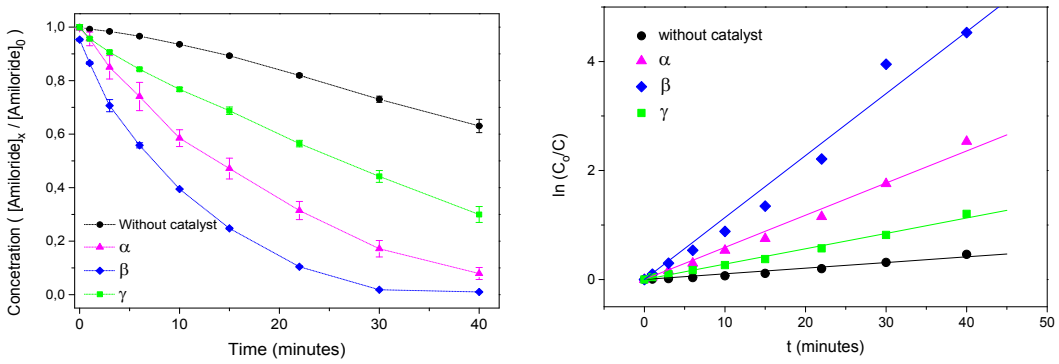

Figure 4. (a) Relative concentration (C/C_o) versus time (min) of AML photocatalytic degradation by α-, β- and γ-Ag_2WO_4 polymorphs under UV irradiation. Photolysis (●); α (▲); β (♦) and γ (■); and (b) Reaction kinetic of AML photodegradation for the different Ag_2WO_4 polymorphs.

The values of the rate constants for the degradation processes are shown in Table 1. An analysis of the results renders that β-Ag_2WO_4 exhibits the highest constant rate with a k value of 0.114 min^{-1}. This k value is 1.9 and 4.1 times that of α- and γ-Ag_2WO_4, respectively. A better efficiency of the metastable β-Ag_2WO_4 compared to the α-Ag_2WO_4 has been reported over dye photodegradation process under visible light [62]. Under UV irradiation, β-Ag_2WO_4 also exhibited higher photocatalytic activity both for methyl orange [56] and phenol and azo-dye X3B [43] degradation than α-Ag_2WO_4 nanorods. The higher photocatalytic performance of β-Ag_2WO_4 can be ascribed to the differences between the surface structures of each faceted morphology. The particular features of the terminal clusters, the electronic distribution, and active sites population for each surface, among others, can be decisive during the adsorption and degradation process. Recently, some heterostrutures have been used for the photodegradation of AML under both visible and UV irradiation[94,95]. These heterostructures, namely g-C_3N_4/Nb_2O_5[94] and

$Bi_2O_2CO_3/BiVO_4$[95], with different weight ratios among their components, were successfully used and have shown higher photoactivity than their isolated phases. Among all the compounds, though, the highest kinetic constant value reported is exceeded 7.72 times by the value found in the present work for the β-Ag_2WO_4.

Table 1. Pseudo-first-order rate constants (k_{app}), correlation coefficients (R^2) and photodegradation efficiencies (PDE) after 30 min for the AML degradation in different Ag_2WO_4 polymorphs.

Samples	k_{app} (min^{-1})	R^2	PDE (%)
Without catalytic	0.0104	0.98	27
α-Ag_2WO_4	0.059	0.99	83
β-Ag_2WO_4	0.114	0.98	98
γ-Ag_2WO_4	0.028	0.99	56

Mechanism of Photocatalytic Activity

In order to further understand the behavior of the photocatalytic activity, an analysis of the PL emissions was carried out so as to investigate the recombination probability of the photogenerated charge carriers. Generally, a weaker PL intensity indicates a lower recombination rate of the photoinduced charges, usually resulting in higher photocatalytic activity. The relevant PL spectra are shown in Figure 5 for all Ag_2WO_4 polymorphs. The PL spectra of β- and γ-Ag_2WO_4 reveal high-energy emission peaks in the two samples with similar narrow shapes around 400–500 nm. Regarding the α-Ag_2WO_4 samples, this peak is not clearly detected due to the presence of a broad and intense low energy emission band with a maximum intensity in the range of 500–800 nm. This result can be reported previously by our research group and this peak can be associated with the presence of the structural disorder and silver

or oxygen vacancies in the $[AgO_x]$ (x = 2, 4, 5, 6, and 7) clusters, which induce more deep defects in the forbidden band gap (defect emissions).[37,48,96] For the α- and β-Ag_2WO_4 samples, the origin of such emissions bands has been clarified.[52] A similar origin can be assumed for γ-Ag_2WO_4. As Figure 5 shows, the emission peaks of the α- and γ-Ag_2WO_4 crystals are the strongest, indicating that the recombination rate of the photogenerated electron (e') and hole ($h^{\bullet}$) pairs is the largest one. Compared to the PL emission peaks of the α- and γ-Ag_2WO_4 crystals, the PL intensity of β-Ag_2WO_4 at the range of 400–466 nm is the weakest one, predicting that the charge combination rate of the photogenerated e'–$h^{\bullet}$ pairs could be further reduced.

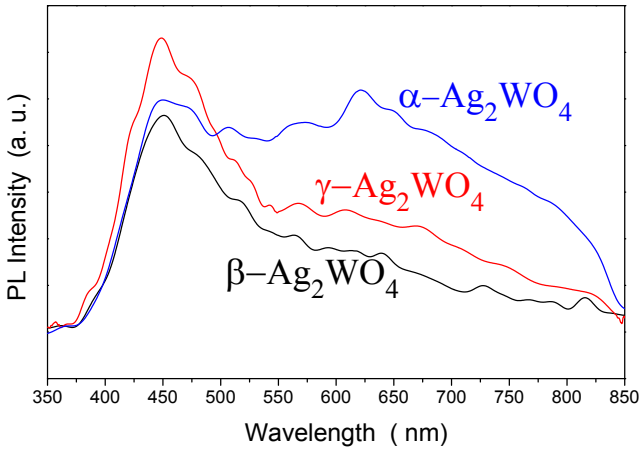

Figure 5. PL spectra for the different Ag_2WO_4 polymorphs.

An XPS analysis was performed in order to identify the chemical composition of the surface, the chemical environment (binding energy) and the oxidation state of the elements. The photoelectron peaks of Ag, W, and O elements are clearly presented in the expanded scan of the XPS spectrum in the range from 0 to 1200 eV, as shown in Figure 6a. The C1*s* peak is due to the adventitious hydrocarbon from the XPS instrument itself. As shown in Figure 6b, the two characteristic peaks, located between 365.7-367.4 eV and 371.75-373.45

eV, could be assigned to Ag $3d_{5/2}$ and Ag $3d_{3/2}$, respectively. The peaks in α-Ag_2WO_4 are slightly located towards higher bending energies, whereas the peaks in β-Ag_2WO_4 and γ-Ag_2WO_4 shift to a lower binding energy, indicating the variation of the Ag surface state on the different Ag_2WO_4 polymorphs. For all samples, no other peaks were observed in this range, which suggested that metallic Ag^0 is not formed during preparation. The spectrum of W 4*f* shown in Figure 6c shows the typical two well-resolved spin-orbit split peaks related to the binding energy of W $4f_{7/2}$ and W $4f_{5/2}$ states, as it was reported recently in the literature.[97,98]

According to the literature, the binding energies of W with different valences are arranged as follows: $E(W^{6+}) > E(W^{5+}) > E(W^{4+})$, while the difference between them is ~1.5 eV [99]. In α-Ag_2WO_4, there were two peaks toward the higher binding energy values among all polymorphs, at 34.5 eV and 36.5 eV. These bands could be assigned to W^{6+} oxidation state. For β-Ag_2WO_4, the two peaks of W 4*f* were located at energy binding values ~1.5 eV lower than the α- peaks, at 32.95 eV and 35 eV, as expected for W^{5+} oxidation state. However, the high-resolution W 4*f* spectrum of γ-Ag_2WO_4 presents two peaks, centering at 31.9 eV and 34.1 eV. A smaller shift in the energy bending position, very close to W^{5+}, is observed in this polymorph regarding the expected typical W^{4+} oxidation state. This change could be related to a highly distorted tetrahedral cluster on the surface of this metastable polymorph.

The peaks in the O1*s* spectrum (Figure 6d) in α- and γ-Ag_2WO_4 are asymmetrical, with a main O1*s* core level peak and an additional smaller tail or shoulder extending toward higher energies. Tentatively, the O1*s* line with this characteristic has been considered in several systems as being formed by two components. This multicomponent approach can be divided into two bands. The low-energy component, generally with a major contribution,

at ~529-530 eV, is ascribed to the crystal lattice oxygen (O^{2-}). The high-energy component could, alternatively, be assigned to surface defects, as oxygen vacancy (V_O), and/or chemisorbed oxygen species, as the surface hydroxyl group (OH). The components associated to OH may be influenced by the presence of oxygen vacancies[100,101,102].

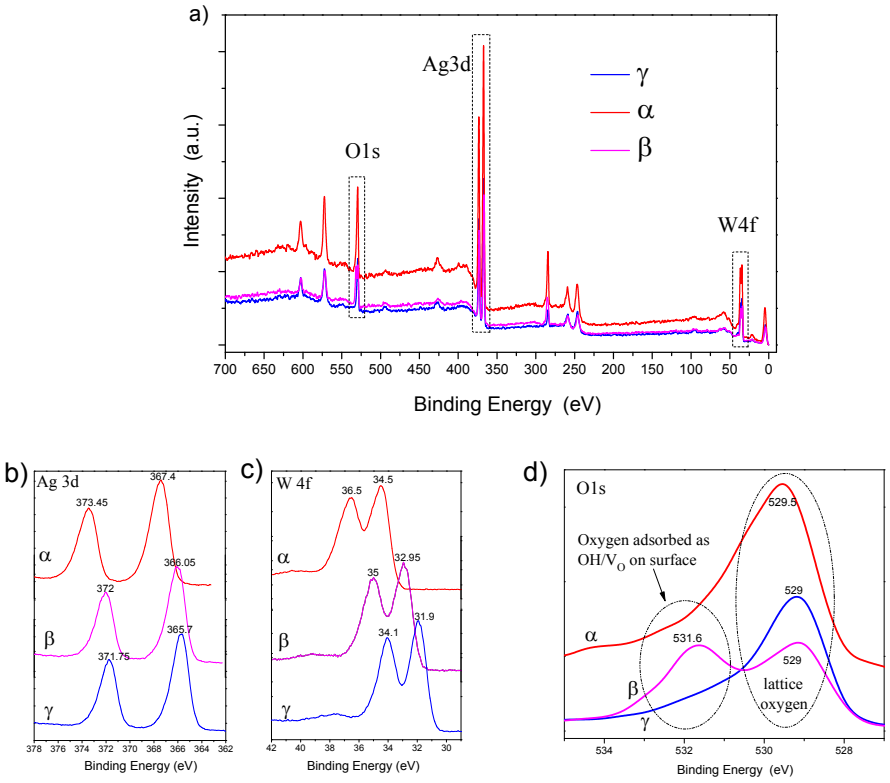

Figure 6. Expanded XPS spectra of α-, β-, and γ-Ag_2WO_4 nanocrystals (a); and high-resolution XPS spectra of: Ag3d (b), W4f (c), and O1s (d) for each Ag_2WO_4 polymorph.

For β-Ag_2WO_4, the intensity of the peak at high-energy, at 531.6, clearly increases. This can imply that more V_O and/or OH groups in the surface of this polymorph can appear and contribute to its photocatalytic reactions. Different authors have pointed out that the presence of V_O and/or OH plays an active role during surface reaction phenomena[103,104,105,106,107]. According to the results above, we suggest that V_O and/or OH on

the surface of β-Ag_2WO_4 photocatalyst could improve the photoactivity of the AML degradation process.

With the purpose of further explore the mechanism of AML photodegradation, trapping experiments were carried out to identify which reactive species take part in the degradation process. AA, IPA, and AO scavengers for O_2', radical OH^*, and $h^\bullet$, respectively, were added to the photocatalytic system and results are shown in Figure 7. In addition, in order to know how much each of the scavengers inhibits the photodegradation a "blank" containing AML only and the polymorphs without any scavenger was also performed.

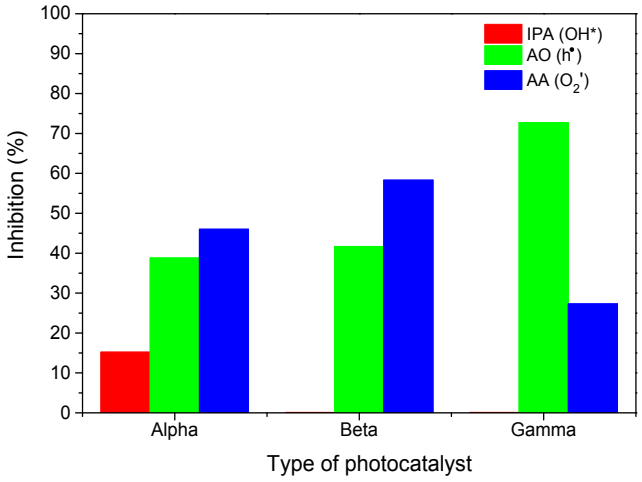

Figure 7. Effects of different radical scavengers on AML degradation in α-, β- and γ-Ag_2WO_4 polymorphs under UV irradiation.

An analysis of the results included in Figure 7 shows a decrease in the photodegradation efficiency with the addition of all the scavengers. The decrease was more pronounced when adding AA and AO, implying that O_2' and $h^\bullet$ play an important role in the photodegradation process in the α- and β-polymorphs, while the γ-phase shows a less efficient photodegradation process with the participation of $h^\bullet$. It should be noted that OH^*

radicals were not the dominant active species. After gathering the XPS analysis and scavenger tests, we can suggest that the photogenerated $h^{\bullet}$ in the valence band are trapped by the surface OH^- group to produce the hydroxyl radical, OH^*, while the e' in the conduction band are taken up by the molecular oxygen, O_2, to generate superoxide radical O'_2, which can be considered the most important species in the photocatalytic activity.

In catalytic applications, the structural stability of a photocatalyst is a crucial parameter. After the photocatalytic process, the photocatalysts were separated from the solution by centrifugation between experiments. Later on, they were collected and the Ag_2WO_4 polymorphs were identified through XRD analyses. The patterns, displayed in Figure 8a, showed that the characteristic diffraction peaks of all the samples still exist, which indicates certain photochemical stability of the three photocatalysts. Remarkably, for the β- and γ-phases, a relatively weak diffraction peak located at 2θ=38.1 degrees (see Figure 8b), which correspond to the (111) lattice plane of Ag (JCPDS no. 65-2871), was detected. However, this diffraction peak does not appear for the α-Ag_2WO_4.

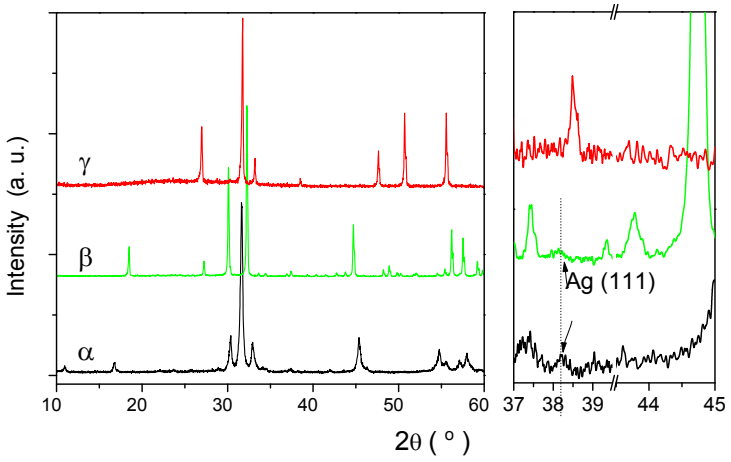

Figure 8. XRD of α-, β-, and γ-Ag_2WO_4 microcrystals after photocatalysis process (a). An amplification of corresponding Ag^0 (111) lattice plane is shown in (b).

Other characteristic diffraction peaks of Ag located at $2\theta^{o}$=44.3, which correspond to the (200) plane, were not observed, confirming that the Ag phase is present in very little concentration. This behavior can be understood in terms of a possible capture of some photoexcited electrons by Ag^{+} ions to form metallic Ag^{0} in the Ag_2WO_4 surface, as reported by our group for Ag-based materials under electron beam irradiation[40,64, 96,108,109,110,111,112,113].

Antibacterial activity

Through the counting of colony forming units per mL (CFU/mL) similar antibacterial activity was observed between the β- and γ-phases, which, in turn, were superior to that in its α-phase. As Figure 9 shows, the MBC values found for the materials were 62.5 μg/mL for α-Ag_2WO_4, and 31.25 μg/mL for β- and γ-Ag_2WO_4. It can also be observed that, even in the sub-inhibitory concentrations, all materials showed a reduction in the amount of microorganisms when compared with the control.

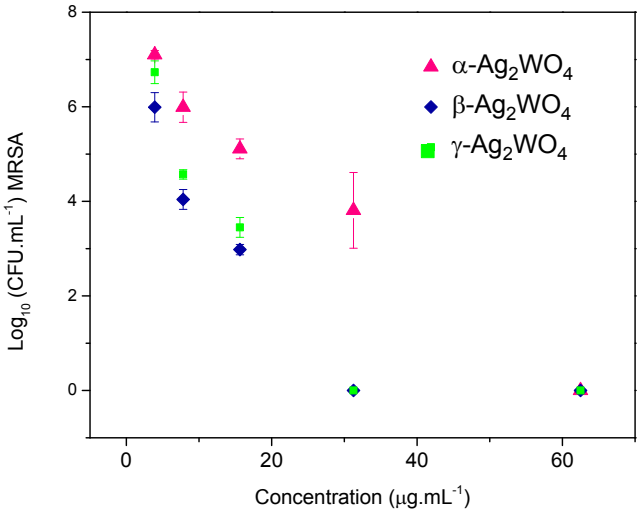

Figure 9. Summary of $\log_{10}$ CFU/mL MRSA values for inhibitory and sub-inhibitory concentrations of α, β and γ-Ag_2WO_4. Control MRSA = 8.21 (± 0.94) log10 CFU/mL.

The effects of the treatment with Ag_2WO_4 were analyzed through SEM microscopy images. Figure 10 shows a significant reduction in the amount of MRSA cells in the groups treated with α-Ag_2WO_4 (Figure 10b), β-Ag_2WO_4 (Figure 10c) and γ-Ag_2WO_4 (Figure 10d) in relation to the control (Figure 10a). Morphological changes in the cells in contact with the materials cab be observed, which appear with a shriveled surface.

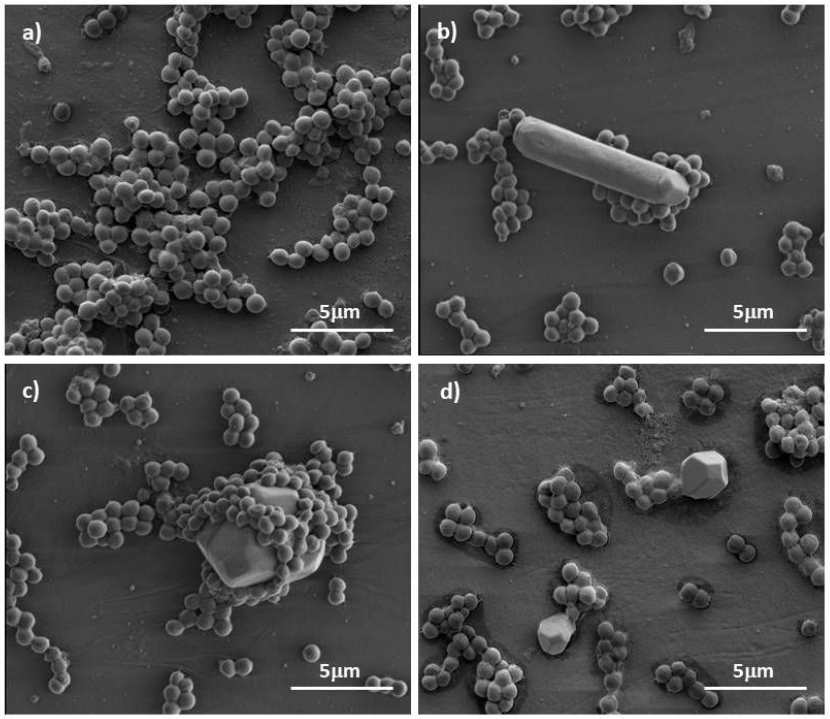

Figure 10. FE-SEM micrographs of MRSA: (a) untreated and treated with (b) α-; (c) β- and (d) γ-Ag_2WO_4.

The confocal laser microscopy images corroborate the findings in FE-SEM and CFU/mL, as shown in Figure 11. In comparison to the control (Figure 11a), all materials were effective in eradicating MRSA. When treated with the materials in β- and γ-phases, MRSA culture presents greater damage compared to the group treated with the α-phase of

the material. Bacterial viability was monitored by the damage to the cell membrane caused by the treatments. When the cells had their membrane compromised, they were marked in red and considered dead, or in the process of death. When they had their membrane intact, they were marked in green and considered alive. Although β- and γ-phases showed similar antibacterial activity, it is possible to observe a greater number of non-viable cells in the bacterial culture treated with the β-Ag_2WO_4 (see Figure 11c).

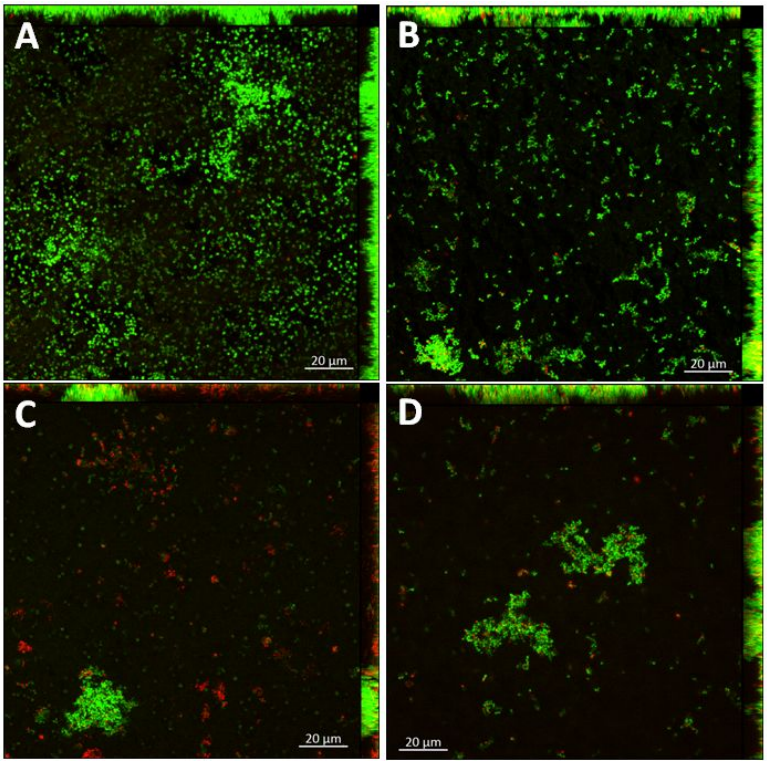

Figure 11. MRSA confocal laser scanning microscopy images: (a) untreated and treated with (b) α-; (c) β- and (d) γ-Ag_2WO_4.

As a result of the metabolism and respiration of aerobic beings, low levels of ROS such as superoxide (O_2') and hydrogen peroxide (H_2O_2) are produced. Although the cells have defense mechanisms against them, through superoxide dismutase and catalase, high concentrations of O_2' and H_2O_2 overload the defense mechanisms of microbial cells, making

them highly susceptible to other ROS, such as OH^* and singlet oxygen ($^1O_2$)[114]. Semiconductor materials, such as Ag_2WO_4, are known to have the ability to release ROS. These, in turn, when in contact with microorganisms, are responsible for membrane damage, which lead them to death [40,115]. Specifically in bacteria, proteins are affected by the rapid rates of reaction with ROS[114].

Morphology and surfaces analysis

Most chemical reactions involved in the photocatalytic and antibacterial activity do not occur in a bulk phase, but at a surface or interface. Their efficiency is strongly dependent on the exposed surfaces, which possess different atomic configurations and electronic properties. Modify charge transfer processes ultimately result in distinct abilities. Then, the interplay between molecules/bacteria and active sites on the topmost surface of solid semiconductors determines their photocatalytic and antibacterial potential. These surface effects can be explained by three viewpoints: (i) may generate ROS or (ii) may release metal ions, to destroy bacterial DNA and protein; and (iii) may gather nanoparticles on the surface of the bacterial cell membrane and, thus, destroy the cell membrane and interrupt transmembrane electron transfer[116,117].

Figure 12a-c shows a number of FE-SEM images of the pure Ag_2WO_4 polymorphs under the experimental conditions. The analysis of images shows that all samples are composed mainly of micro-sized particles. A wide particle size distribution can be observed. The final morphologies respond to the intrinsic anisotropic growth habits of the three polymorphs. The morphology of the α-Ag_2WO_4 orthorhombic structure is composed by the (010), (001) and (101) surfaces, while for the β-Ag_2WO_4 hexagonal structure it is formed by the (110) and (011) surfaces. The morphology of the γ-Ag_2WO_4 cubic structure

is composed by (001), (011), and (111) surfaces. Table 2 shows, for each crystal morphology, the values of E_{surf}, percentage contribution (% cont.) of each surface, $E_{gap}^{surface}$, $E_{polyhedron}$, and $E_{gap}^{polyhedron}$.

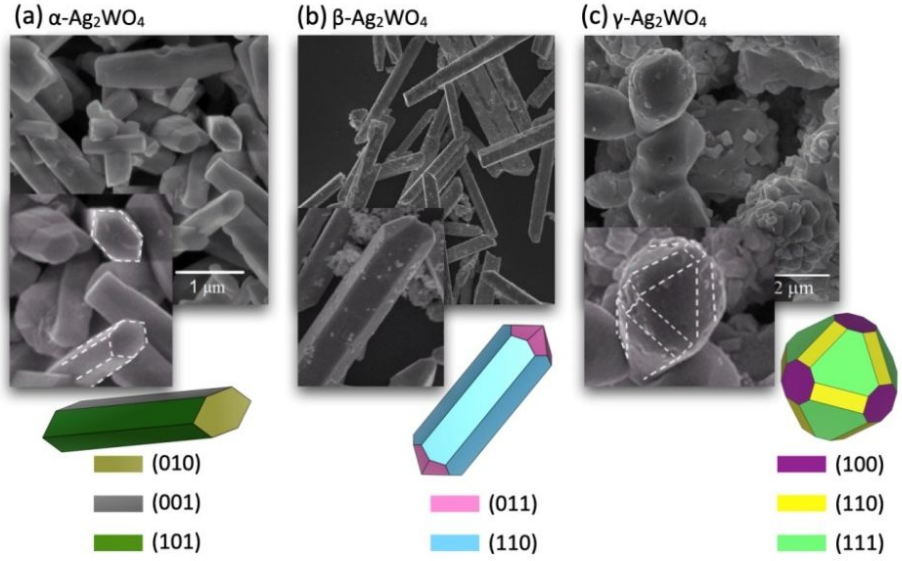

Figure 12. Experimental FE-SEM images of (a) α-Ag_2WO_4, (b) β-Ag_2WO_4, and (c) γ-Ag_2WO_4 polymorphs synthesized at different precursors concentration ratio. The theoretical morphologies are included for comparison purposes.

The theoretical morphologies in Figure 12 were obtained by changing the stability of the surfaces that formed the theoretical morphology (ideal), i.e., by increasing/decreasing the calculated values of the E_{surf}. The information about the ideal morphologies can be found in Table SI-1 (see Supporting Information). By adjusting the ratio of the E_{surf} values of each surface in each polymorph, the complete map of available morphologies can be obtained[66,68,77].

Table 2. Surface energy (E_{surf}, J/m^2), percentage contribution (% cont.) of each surface for the experimental morphology, band gap energy for each surface ($E_{gap}^{surface}$, eV), polyhedron energy of each experimental morphology ($E_{polyhedron}$, J/m^2), and the band gap energy of each experimental polyhedron ($E_{gap}^{polyhedron}$, eV).

Morphology	E_{surf}	% cont.	$E_{gap}^{surface}$	$E_{polyhedron}$	$E_{gap}^{polyhedron}$
α-Ag_2WO_4 $E_{gap}^{bulk} = 1.69eV$	(010) – 0.80	14%	1.39	0.35	1.01
	(001) – 0.20	36%	0.65		
	(101) – 0.32	50%	1.15		
β-Ag_2WO_4 $E_{gap}^{bulk} = 1.62eV$	(011) – 0.22	19%	1.61	0.11	1.62
	(110) – 0.08	81%	1.62		
γ-Ag_2WO_4 $E_{gap}^{bulk} = 1.84eV$	(100) – 1.23	20%	1.84	1.13	1.57
	(110) – 1.17	28%	1.37		
	(111) – 1.07	52%	1.58		

The energy profile connecting the ideal (obtained directly from the relation of the surface energies values and the Wulff construction) and theoretical (coinciding with the experimental FE-SEM images) is obtained by calculating the $E_{polyhedron}$, as shown in Figure 13. This procedure can be considered an effective tool to investigate the mechanisms of morphology transformation and crystal growth from a thermodynamic and kinetic point of view[53].

The ideal morphology of α-Ag_2WO_4 is formed by the (001), (010), and (100) surfaces with a parallelepiped-like shape. To achieve the experimental FE-SEM morphology, the α-Ag_2WO_4 passes along the A-D intermediate morphologies. Therefore, it is first necessary to increase the E_{surf} of the (010) surface (morphology A), followed by an E_{surf} increase of the (100) surface, to obtain morphology B. These two steps increase the value of

$E_{polyhedron}$, which results in a point of maximum. The next two steps involve the decrease of the E_{surf} in the (001) surface (morphology C) and the increase of the E_{surf} in the (110) surface (morphology D). From here, a last decrease in the (101) surface takes place in order to obtain the experimental morphology.

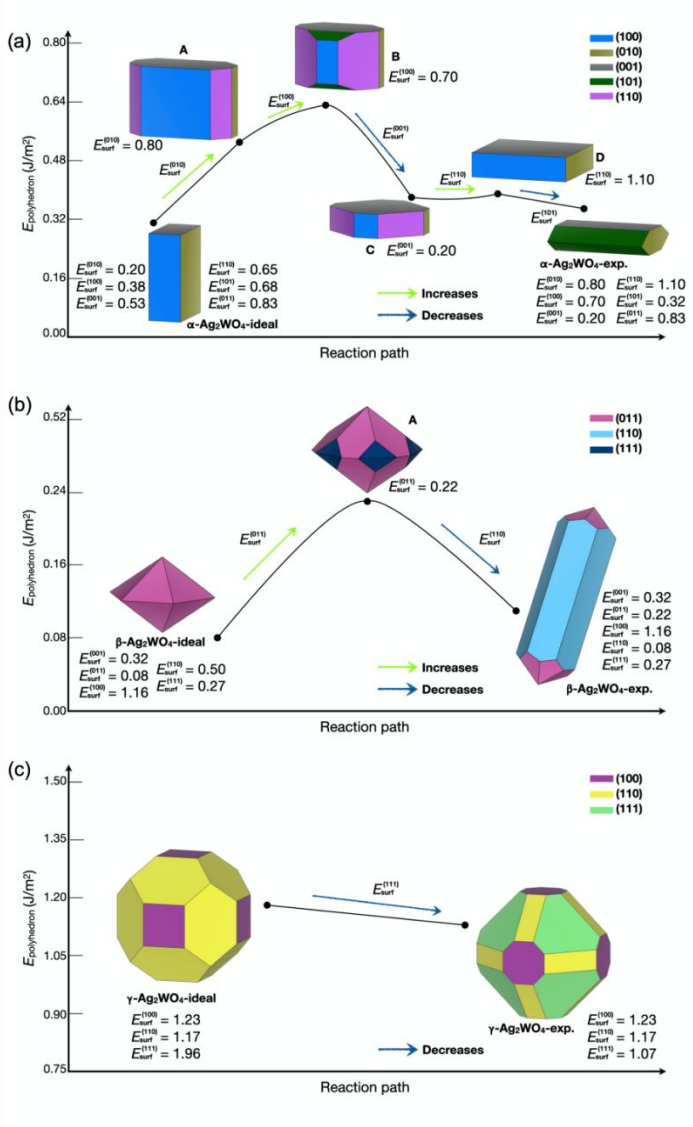

Figure 13. Polyhedron energy profile connecting the theoretical (ideal) and experimental morphologies: (a) α-Ag_2WO_4, (b) β-Ag_2WO_4 and (c) γ-Ag_2WO_4. Values of E_{surf} in J/m^2. The intermediate morphologies along the pathways are indicated with letters.

In the case of β-Ag_2WO_4, the reaction path to go from ideal to experimental FE-SEM images takes place along one maximum (morphology A), involving an E_{surf} increase in the (011) surface followed by an E_{surf} decrease in the (110) surface. In the γ-Ag_2WO_4 polymorph it is only necessary to decrease the E_{surf} value in the (111) surface to connect the ideal to the experimental morphology observed in the FE-SEM analyses.

Connecting morphology and activity

It is known that the properties of the materials are morphology dependent. Exposed surfaces are the interface between a material and its environment. The interplay between molecule/bacteria and active sites on the topmost surface of solid determines its activity in heterogeneous catalysis and as antibacterial agent. Thus, it is essential to characterize, in as much detail as possible, the surface structure and electronic properties of materials to rationalize both adsorption and degradation processes at the exposed surface of the three polymorphs. Unfortunately, the experimental techniques often adopted for such characterization are not sensitive enough to solid' topmost surface. With the support of calculations, the type of atoms, structure, and electronic characteristics of the clusters at the top of each surface were found facet-dependent, which affects the activation of the adsorbed AML and MRSA significantly. This type of analysis allows us to find an adequate relationship between structure-function. Figure 14 shows the geometries of the exposed surfaces for the different polymorphs. The use of the Kröger-Vink notation[118] makes possible to analyze the number of Ag−O and W−O breaking bonds in the superficial clusters. Each surface presents different kinds of atoms and local coordination on the top of

the surface, together with the presence of complete coordinated and undercoordinated clusters and neutral oxygen vacancies (represented by V_o^x).

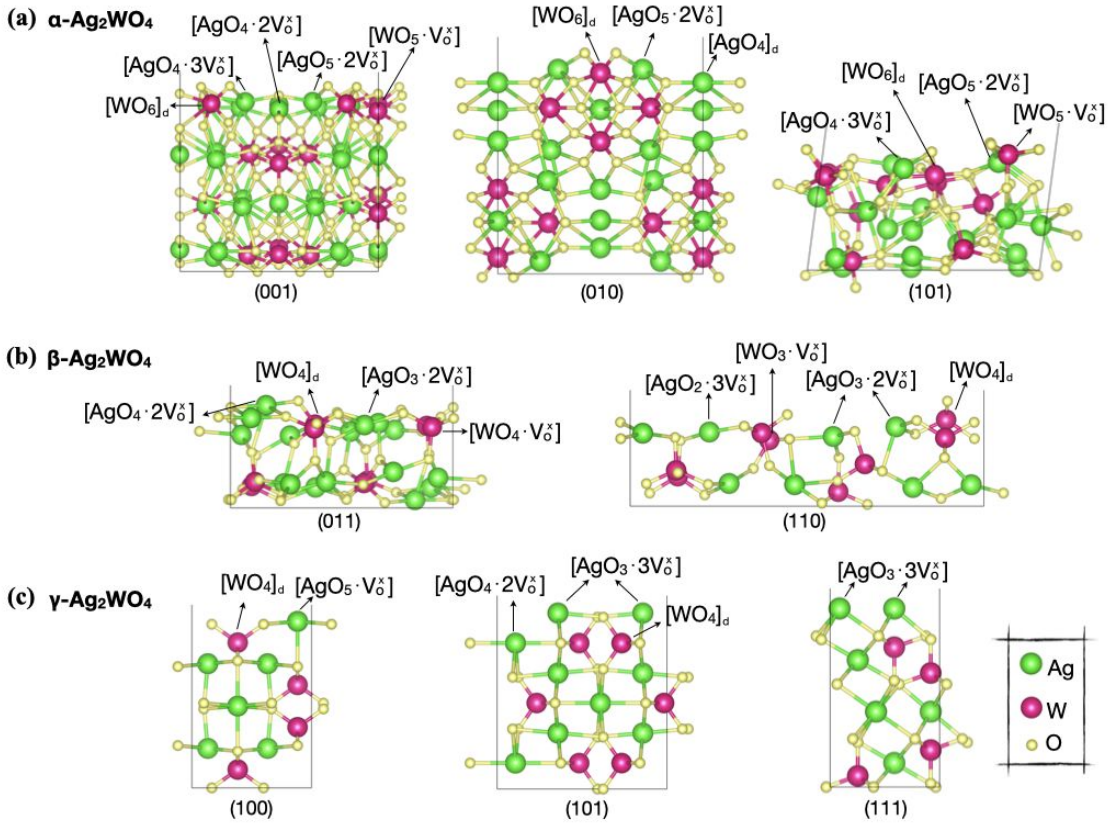

Figure 14. Representation of the exposed surfaces of each Ag_2WO_4 polymorphism: **(**a) α-Ag_2WO_4, (b) β-Ag_2WO_4 and (c) γ-Ag_2WO_4. The undercoordinated clusters of Ag and W cations are highlighted.

As Figure 14a shows, all α-Ag_2WO_4 surfaces display the $[WO_6]_d$ and $[AgO_5{\cdot}2V_o^x]$ clusters on the top of the surface, where the sub index "d" means distorted. The (010) surfaces also present $[AgO_4]_d$ clusters. The (001) and the (101) surfaces present $[AgO_4{\cdot}3V_o^x]$ and $[WO_5{\cdot}V_o^x]$ clusters, while on the (001) surfaces the $[AgO_4{\cdot}2V_o^x]$ clusters appear too. The (011) and (110) surfaces of the β-Ag_2WO_4 (Figure 14b) are formed by the $[WO_4]_d$ and

$[AgO_3{\cdot}2V_o^x]$ clusters. Beyond these two kinds of clusters, in the (011) surface there are also $[AgO_4{\cdot}2V_o^x]$ and $[WO_4{\cdot}V_o^x]$ clusters. In the (110) surface, the $[AgO_2{\cdot}3V_o^x]$ and $[WO_3{\cdot}V_o^x]$ clusters are presented too. On the γ-Ag_2WO_4 surfaces (see Figure 14c), the (100) surface is constituted by distorted $[WO_4]_d$ and undercoordinated $[AgO_5{\cdot}V_o^x]$ clusters. The top of the (101) surface is formed by three different kind clusters: $[WO_4]_d$, $[AgO_3{\cdot}3V_o^x]$ and $[AgO_4{\cdot}2V_o^x]$. The (111) surface is the most organized structure. The top of this surface is formed exclusively by undercoordinated $[AgO_3{\cdot}3V_o^x]$ clusters.

When compared to ideal morphologies, the appearance in the experimental morphology of a new surface, namely (101) in α-Ag_2WO_4 and (110) in β-Ag_2WO_4 crystals (as seen in Figure 13), is a related fact that follows the existence of undercoordinated W atoms on the top the surface: $[WO_5{\cdot}V_o^x]$ in (101) and $[WO_3{\cdot}V_o^x]$ in (110). However, for γ-Ag_2WO_4, the (111) surface of its experimental morphology presents a majorly exposed surface with only $[AgO_3{\cdot}3V_o^x]$ clusters. The undercoordination of $[WO_y]$ clusters in a surface usually generates more instability than $[AgO_x]$ clusters, whose surfaces are stabilized under experimental conditions to be exposed in the final morphology. Thus, the (101) surface with one oxygen vacancy of the octahedral $\left[WO_5{\cdot}V_o^x\right]$ cluster in the α-Ag_2WO_4 and the (110) surface with one oxygen vacancy of the tetrahedral $[WO_3{\cdot}V_o^x]$ cluster in the β-Ag_2WO_4 morphology seems to be the most active surfaces for the corresponding polymorph.

Table 2 gathers the E_{gap} values of the bulk, surfaces and each morphology ($E_{gap}^{polyhedron}$) for α-, β- and γ-Ag_2WO_4 crystals correlated to their E_{surf}. In passing from 6-faceted crystal (prism) to 8-faceted crystal (rod-like) of α-Ag_2WO_4, the $E_{gap}^{polyhedron}$ shows a slight variation from 0.99 to 1.01 eV. At the same time, surface (100) disappears and the (101)

surface gains importance. In the case of the β-Ag_2WO_4 phase, the $E_{gap}^{polyhedron}$ variation from ideal to experimental morphology is minimum, from 1.61 to 1.62 eV, but higher in value than in the α-Ag_2WO_4 phase. Computational calculations indicate that the morphology of the β-Ag_2WO_4 crystal has the (011) surface as the predominantly exposed surface. By adjusting the relation of the E_{surf} values in order to obtain the experimental morphology, the (110) surface plays an important role in the overall morphology, more so than the (011) surface, with similar band gap energy values. For γ-Ag_2WO_4, in passing from ideal to experimental morphology, the $E_{gap}^{polyhedron}$ value increases from 1.46 to 1.57 eV due to the appearance of the (111) surface. However, the β-Ag_2WO_4 crystal presents a low E_{gap} bulk value (1.62 eV) compared to the α and γ-phases (1.69 and 1.84 eV, respectively) conferring β-Ag_2WO_4 crystals a better ability to act as active sites for AML degradation, since a low recombination rate between photogenerated e' and $h^{\bullet}$ on the crystal surface can be produced.

The main responsible factor for both the photocatalytic and the antibacterial activity is a low recombination rate between photogenerated e'-$h^{\bullet}$ pairs on the surface of the Ag_2WO_4 polymorphs. The photogenerated charges undergo a series of redox reactions with oxygen molecules, O_2, and water, H_2O, on the surface to generate ROS with extreme chemical activity. The $h^{\bullet}$ on the surface reacts with H_2O, to yield OH^* and the $H^{\bullet}$ radicals, while the e' can be trapped by O_2 adsorbed on the surface to generate O_2' radicals:

$$h^{\bullet} + H_2O \rightarrow OH^* + H^{\bullet} \quad (6)$$

$$e' + O_2 \rightarrow O_2' \quad (7)$$

These OH^* and O_2' radicals induce the degradation of AML and the antibacterial activity.

An analysis of the results gathered in Table 2 shows that the (101) and (001) surfaces are the main components, 50% and 36%, respectively, of α-Ag_2WO_4 morphology. On the (101) surface there is an accumulation of e' in the complete distorted $[WO_6]_d$ clusters together with e' depletion and positive charge accumulation in the undercoordinated $[AgO_5{\cdot}2V_o^x]$, $[AgO_4{\cdot}3V_o^x]$ and $[WO_5{\cdot}V_o^x]$ clusters, creating a potential difference which is able to form a local electric field. These differences in the charge of the different clusters on the surface have an influence on the transfer of the photogenerated e'-$h^\bullet$ to the outside. On the (001) surface, this charge separation process is from distorted $[WO_6]_d$ clusters to undercoordinated $[AgO_4{\cdot}3V_o^x]$, $[AgO_4{\cdot}2V_o^x]$, $[AgO_5{\cdot}2V_o^x]$, and $[WO_5{\cdot}V_o^x]$ clusters. For β-Ag_2WO_4, the exposed (110) surface represents 81% of its morphology, e'-$h^\bullet$ separation taking place from the distorted $[WO_4]_d$ cluster to the undercoordinated $[AgO_3{\cdot}2V_o^x]$, $[AgO_2{\cdot}3V_o^x]$, and $[WO_3{\cdot}V_o^x]$ clusters. This makes β-Ag_2WO_4 the most active polymorph out of the three. The results indicate that the exposed surfaces can enhance the migration of photoinduced e', suppressing the recombination of charge carriers and improving the antibacterial and photocatalytic activity. Thus, it can be concluded that the source of $h^\bullet$ is the undercoordinated $[AgO_x \cdot zV_o^x]$ and $[WO_y \cdot zV_o^x]$ clusters, while the source of e' is the distorted $[WO_y]_d$ clusters. The following mechanisms for the photocatalytic and antibacterial activity can be concluded:

$$[AgO_x \cdot zV_o^x] + H_2O \rightarrow OH^* + H^\bullet \quad (8)$$

$$[WO_y \cdot zV_o^x] + H_2O \rightarrow OH^* + H^\bullet \quad (9)$$

$$[WO_y]_d + O_2 \rightarrow O_2' \quad (10)$$

Formation Mechanisms of Ag_2WO_4 polymorphs

Both the intimate mechanisms behind the structural evolution process from the reagents/precursors to intermediate samples and the formation of the final product's 3D structure in solution are far from being well understood. For inorganic solids, structural and bonding analyses during crystal synthesis are particular complex and are usually ambiguous at the atomic scale. This is partially due to the lack of efficient real-time methods of identifying all the chemical species, the *in situ* formed intermediates, and reactions involved. Here, an attempt has been made to put forward a formation mechanism of Ag_2WO_4 polymorphs from precursors, as a function of solution chemistry.

The formation of a solid includes the nucleation and growth steps. Nucleation is a kinetically controlled process during which atoms, ions, and/or molecules aggregate into small clusters, at the beginning in a reversible way until they form stable nuclei. The latter are then able to grow into crystallites and crystals. Nucleation *via* intermediate states is typical of a two-step nucleation mechanism, along a non-classical nucleation mechanism.

The crystallization process generally involves a very complex sequence of steps, including the formation of primary units via dissolution, hydration/dehydration, nucleation, and crystal growth. There are multiple complex equilibria between transient species that occur rapidly in solution, which favors the prevalence of some building-blocks over others. However, neither the nucleation reaction pathways nor the nature of the building blocks can be controlled.

In a typical precipitation method, the precursor salts are dissolved in an aqueous environment. In this aqueous solution, the dissolution process is very fast and the corresponding ions are quickly solvated by the H_2O molecules along a barrierless process. $Na_2WO_4 \cdot 2H_2O$ and $AgNO_3$ were the starting materials. First, $Na_2WO_4 \cdot 2H_2O_{(aq)}$ was

dissolved to form $(WO_4)^{2-}_{(aq)}$, Eq. 11, while $AgNO_3$ was dissolved to form Ag^+, which forms the $(Ag(H_2O)_6)^+_{(aq)}$ complex in aqueous solutions (Eq. 12). These two equations represent the dissolution processes, step 1, in which $(WO_4)^{2-}_{(aq)}$ is the precursor of the $[WO_y]$ clusters, Eq. 13, while $(Ag(H_2O)_6)^+_{(aq)}$ is the precursor of $[AgO_x]$ clusters, Eq. 14. At this stage, dissolution/dehydration/nucleation processes take place with the concomitant formation of the $[AgO_x]$ (x =2, 4, 5, 6, and 7) and $[WO_y]$ (y = 4, 5 and 6) clusters as structural precursors to form the 3D lattice of Ag_2WO_4 in the solid state, Eq. 15-17. These clusters, which can be considered the structural entities preceding nucleation, are often coined prenucleation clusters[119,120].

Increasing evidence has shown that nucleation pathways involving disordered pre-nucleation species exist in the crystallization process of inorganic materials. The collision and aggregation of these clusters, which contain more solute (and solvent) molecules than their surrounding environment, are not only able to form a large amorphous phase, but also have influence on the nucleation kinetics to rearrange and render a 3D crystalline phase first, and then a polymorphic selection[24,26,30,119,121]. In this context, we can suggest that the clusters in the reaction environment preceding the nucleation process, step 2, will strongly influence the formation mechanism and subsequently the formation of the as-synthetized polymorphs.

In the present case, the concentration of precursors in the stoichiometric ratio of 2:1 controls the reaction pathway of the nucleation, step 1, to obtain the different Ag_2WO_4 polymorphs, while the crystallization process of these polymorphs, stage 3, involves the formation of $[AgO_x]$ x = 5, 6 and $[WO_y]$ y = 4, 5, and $[AgO_x]$ x = 2, 4, 6, and 7 and $[WO_6]$ clusters, respectively.

At the concentration of $AgNO_3$:$Na_2WO_4 \cdot 2H_2O$ equal to 0.33:0.165, $[AgO_6]$ and $[WO_4]$ clusters are formed, and the γ-Ag_2WO_4 polymorph is reached, Eq. 15. At concentrations of $AgNO_3$:$Na_2WO_4 \cdot 2H_2O$ equal to 0.04:0.02 and 0.007:0.0035, β- and α-Ag_2WO_4 polymorphs, respectively, are selectively obtained, Eq. 16 and 17. In Figure 15 a schematic representation is displayed.

$$Na_2WO_4 \cdot 2H_2O \rightarrow (WO_4)^{2-}_{(aq)} + 2H_2O_{(l)} + 2Na^{+}_{(aq)} \quad (11)$$

$$AgNO_{3(aq)} \rightarrow (Ag(H_2O)_6)^{+}_{(aq)} + (NO_3)^{-}_{(aq)} \quad (12)$$

$$(WO_4)^{2-}_{(aq)} \rightarrow [WO_y],\ y = 4,5,6 \quad (13)$$

$$(Ag(H_2O)_6)^{+}_{(aq)} \rightarrow [AgO_x],\ x = 2,4,5,6,7 \quad (14)$$

$$[AgO_6] + [WO_4] \rightarrow \downarrow \gamma - Ag_2WO_{4(s)} \quad (15)$$

$$[AgO_x],\ x = 5,6 + [WO_y],\ y = 4,5 \rightarrow \downarrow \beta - Ag_2WO_{4(s)} \quad (16)$$

$$[AgO_x],\ x = 2,4,6,7 + [WO_6] \rightarrow \downarrow \alpha - Ag_2WO_{4(s)} \quad (17)$$

It is clear that, in crystals of Ag_2WO_4 polymorphs precipitated and grown under selected reaction conditions, when the concentration of both $AgNO_3$ and $Na_2WO_4 \cdot 2H_2O$ precursors is reduced and their ratio is modified, both the obtained polymorphs and the corresponding morphologies change. It is also known that the energy barrier for nucleation is lower up on increasing the solution concentration, and so crystals tend to nucleate more rapidly. Nucleation in such solutions leads to the formation of γ-Ag_2WO_4 polymorph. However, the nucleation in diluted solutions has a slower growth and so disordered crystals may be obtained, i.e., α- and β-Ag_2WO_4 polymorphs.

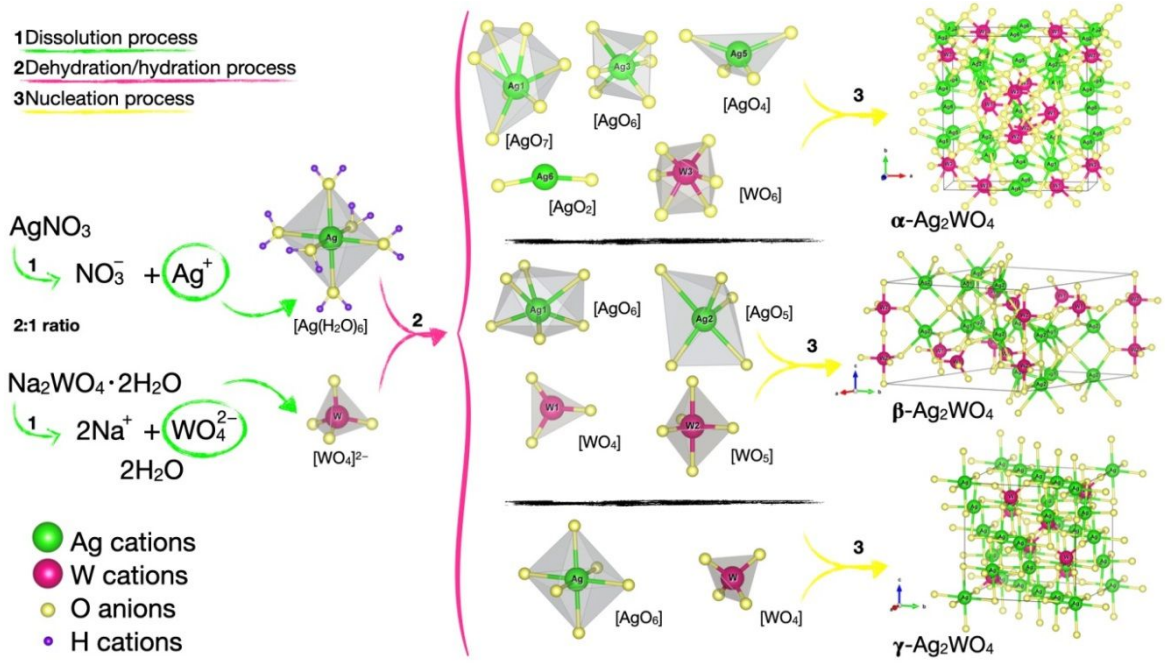

Figure 15. Dissolution/dehydration/nucleation processes for the formation of the different Ag_2WO_4 polymorphs.

This is an example where, at low concentration of precursors, the probability of the formation of disordered clusters with low symmetry at the medium and short range, i.e., the constituent clusters, the formation of $[AgO_x]$, x = 2, 4, 6, 7 and $[WO_6]$, and $[AgO_x]$, x = 5,6 and $[WO_y]$, y = 4,5 of the α-and β-Ag_2WO_4 polymorphs, respectively, is favored. At higher concentration of precursors, the crystallization kinetics process is slower, the effective shocks decrease, greater organization prevails, and symmetry in the crystalline structure, i.e. the appearance of the $[AgO_6]$ and $[WO_4]$ of the γ-Ag_2WO_4 polymorph, is enhanced. This shows that the dominant species in the initial solutions differ and the coordination of ions is also different, affecting the ionic supply to the nucleation centers and consequently promoting the formation of different polymorphs. This implies that the nucleation pathway and crystal precipitation from solutions is a rather complicated process, and aspects such as the solution

components, bond lengths and bond angles of the local coordination of Ag and W cations, $[AgO_x]$, x = 2, 4, 5, 6, 7 and $[WO_y]$, y = 4, 5 and 6, together with oxygen anion coordination and the proximity of ions might affect the crystal morphology and the final formation of each polymorph. Thus, it was possible to assume that several formation mechanisms were involved. A schematic representation of the energy profile along the crystallization progress leading to the obtainment of the 3D structure of the different Ag_2WO_4 polymorphs is proposed in Figure 16. Although the tuning of the microcrystal morphology can be ascribed to these active species and their concentrations, further investigation, such as implementing atomistic simulation techniques to describe the growth kinetics and proper formation pathway of current crystals, is still needed.

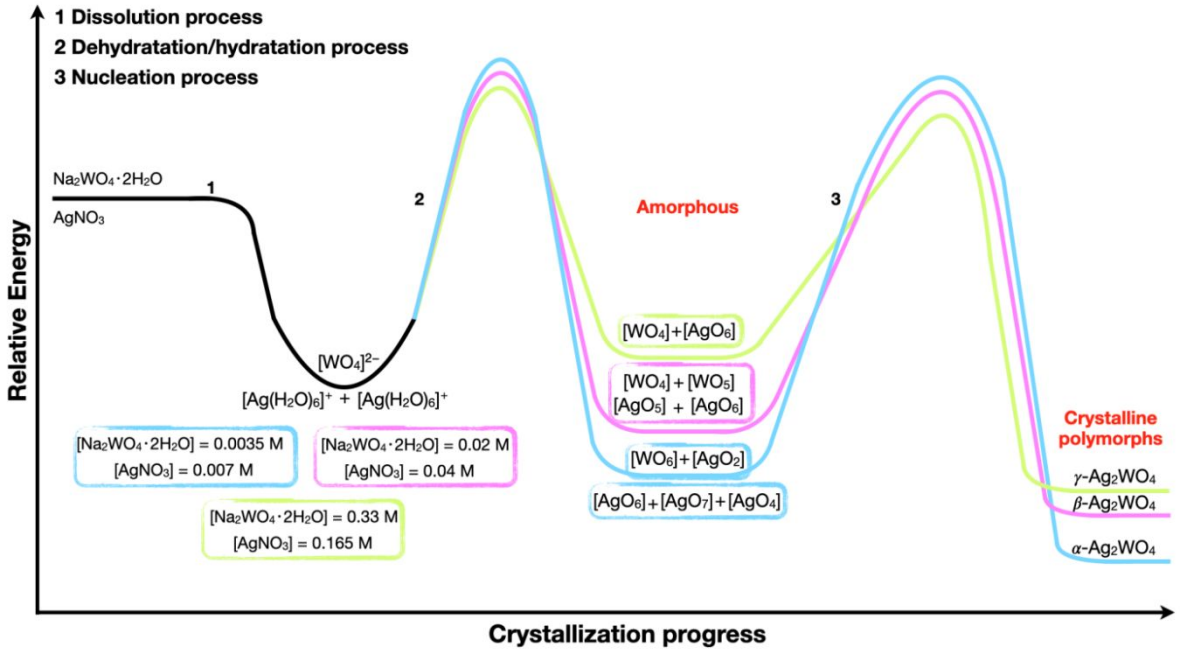

Figure 16. Schematic representation of the energy profiles for the crystallization progress of the different Ag_2WO_4 polymorphs.

CONCLUSIONS AND OUTLOOK

Polymorphism is the ability of solid materials to exist in structurally distinctive arrangements. While displaying the same chemical stoichiometry, with identical repeating formula units, Ag_2WO_4 polymorphs are simply "packed" (or connected) differently, forming various crystal symmetries and lattices with different properties. Therefore, the ability to experimentally control and predict polymorph formation is vital to gain consistent access to its desired applications.

The main conclusions of this work can be summarized as follows: i) The study suggests a procedure that may enable the selective synthesis of α-, β- and γ-Ag_2WO_4 polymorphs without the need of presence of surfactants, which are undesirable in industrial-scale production; (ii) The catalytic mechanism involves the efficient separation of photogenerated $e'/h^{\bullet}$ pairs. The active substance capture tests indicate that two kinds of generated active species (O_2' and $h^{\bullet}$) play an important role in the photodegradation process of α- and β-polymorphs, while in the γ-phase it shows a less efficient photodegradation process with the participation of $h^{\bullet}$; (iii) For the first time, the antimicrobial capacity of Ag_2WO_4 metastable phases is reported. Specifically, the β-Ag_2WO_4 was more effective, requiring half of the concentration for the elimination of the methicillin-resistant *Staphylococcus aureus*; (iv) We demonstrate, building on DFT results, that there is a relation between morphology and photocatalytic/antibacterial activity based on the different numbers of unsaturated superficial Ag and W cations (local coordination, i.e., clusters) of each surface of the three polymorphs; and (v) A mechanism for the crystallization

processes of the three Ag_2WO_4 polymorphs, involving dissolution, dehydratation/hydratation, and nucleation steps is proposed.

Present results provide critical information to expand our fundamental understanding of the precursors' effect along the synthesis of the three polymorphs, a field that has so far remained unexplored. We hope that this study will ultimately help to understand the structural and functional differences between the different kinds of polymorphs and contribute to the development of structure–property relationships in these intriguing Ag_2WO_4-based materials. Further work in extending this protocol and verifying its applicability in other kinds of compounds and chemical transformations is in progress.

SUPPORTING INFORMATION

The following parameters for theoretical morphology are provided in a table: surface energy (J/m^2), percentage contribution (% cont.) of each surface, band gap energy for each surface (eV), polyhedron energy (J/m^2), and the band gap energy (eV).

ACKNOWLEDGMENTS

The authors are grateful to Fundação de Amparo à Pesquisa do Estado de São Paulo (FAPESP- Centro de Desenvolvimento de Materiais Funcionais: 2013/07296-2; FAPESP 2019/13507-2; FAPESP 2016/23891-6; FAPESP 2017/12594-3; FAPESP 2017/19548-7; FAPESP 2019/01732-1). J.A. acknowledges Universitat Jaume I for project, UJI-B2019-30, and Ministerio de Ciencia, Innovación y Universidades (Spain) project PGC2018-094417-B-I00 for supporting this research financially. This work used computational resources of the "Centro de Computação John David Rogers" (CCJDR-UNICAMP). We also wish to

thank the Servei d'Informática, Universitat Jaume I, for their generous allocation of computer time.

REFERENCES

(1) Chieng, N.; Rades, T. . J. A. An Overview of Recent Studies on the Analysis of Pharmaceutical Polymorphs. *J. Pharm. Biomed. Anal.* **2011**, *55*, 618–644.

(2) Wang, Y.; Guan, X.; Li, L.; Lin, H.; Wang, X.; Guangshe, L. Solvent-Driven Polymorphic Control of $CdWO_4$ Nanocrystals for Photocatalytic Performances. *New J. Chem* **2012**, *36*, 1852–1858.

(3) Sanna, S.; Esposito, V.; Andreasen, J. W.; Hjelm, J.; Zhang, W.; Kasama, T.; Simonsen, S. B.; Christensen, M.; Linderoth, S.; Pryds, N. Enhancement of the Chemical Stability in Confined δ-Bi_2O_3. *Nat. Mater.* **2015**, *14*, 500–504.

(4) Yin, B.; Zhang, S.; Jiang, H.; Qu, F.; Wu, X. Phase-Controlled Synthesis of Polymorphic MnO 2 Structures for Electrochemical Energy Storage. *J. Mater. Chem. A* **2015**, *3*, 5722–5729.

(5) Shivaramaiah, R.; Lander, L.; Nagabhushana, G. P.; Rousse, G.; Tarascon, J.-M.; Navrotsky, A. Thermodynamic Properties of Polymorphs of Fluorosulfate Based Cathode Materials with Exchangeable Potassium Ions. *ChemPhysChem.* **2016**, *17*, 3365–3368.

(6) Le Pevelen, D. D.; and Tranter, G. E. FT-IR and Raman Spectroscopies, Polymorphism Applications. In *Encyclopedia of Spectroscopy and Spectrometry*; J. C. Lindon, G. E. T. and D. W. K., Ed.; Academic Press: Oxford, 2017; pp 750–761.

(7) Yogananda, H. S.; Nagabhushana, H.; Naik, R.; Prashantha, S. C. Calcination Temperature Dependent Structural Modifications, Tailored Morphology and Luminescence Properties of MoO_3 Nanostructures Prepared by Sonochemical Method. *J. Sci. Adv. Mater. Devices.* **2018**, *3*, 77–85.

(8) Birgisson, S.; Saha, D.; Iversen, B. B. Formation Mechanisms of Nanocrystalline MnO_2 Polymorphs under Hydrothermal Conditions. *Cryst. Growth Des.* **2018**, *18*, 827–838.

(9) Li, Y.-F.; Liu, Z.-P. Active Site Revealed for Water Oxidation on Electrochemically Induced δ-MnO_2 : Role of Spinel-to-Layer Phase Transition. *J. Am. Chem. Soc.* **2018**, *140*, 1783–1792.

(10) Gentili, D.; Gazzano, M.; Melucci, M.; Jones, D.; Cavallini, M. Polymorphism as an Additional Functionality of Materials for Technological Applications at Surfaces and Interfaces. *Chem. Soc. Rev.* **2019**, *48*, 2502–2517.

(11) Dondur, V.; Markovic, S.; Dimitrijevic, R.; Macura, S.; Arandjelovic, D. Reconstructive and Displacive Transformations of Tectosilicates. Non-Stoichiometric Carnegieite. *J. Therm. Anal. Calorim.* **2003**, *72*, 373–381.

(12) Gebauer, D.; Völkel, A.; Cölfen, H. Stable Prenucleation Calcium Carbonate Clusters. *Science.* **2008**, *322*, 1819–1822.

(13) Hanaor, D. A. H.; Sorrell, C. C. Review of the Anatase to Rutile Phase Transformation. *J Mater Sci.* **2011**, *46*, 855–874.

(14) Sood, S.; Gouma, P. Polymorphism in Nanocrystalline Binary Metal Oxides. *Nanomater. Energy* **2013**, *2*, 82–96.

(15) Kumar, S. G.; Koteswara Rao, K. S. R. Polymorphic Phase Transition among the Titania Crystal Structures Using a Solution-Based Approach: From Precursor Chemistry to Nucleation Process. *Nanoscale.* **2014**, *6*, 11574–11632.

(16) Sun, W.; Jayaraman, S.; Chen, W.; Persson, K. A.; Ceder, G. Nucleation of Metastable Aragonite $CaCO_3$ in Seawater. *Proc. Natl. Acad. Sci.* **2015**, *112*, 3199–3204.

(17) Belsky, A.; Hellenbrandt, M.; Karen, V. L.; Luksch, P. New Developments in the Inorganic Crystal Structure Database (ICSD): Accessibility in Support of Materials Research and Design. *Acta Crystallogr. Sect. B Struct. Sci.* **2002**, *58*, 364–369.

(18) Zwijnenburg, M. A.; Illas, F.; Bromley, S. T. Apparent Scarcity of Low-Density

Polymorphs of Inorganic Solids. *Phys Rev Lett.* **2010**, *2010*, 175503.

(19) Jansen, M.; Pentin, I. V.; Schön, J. C. A Universal Representation of the States of Chemical Matter Including Metastable Configurations in Phase Diagrams. *Angew. Chem. Int. Ed.* **2012**, *51*, 132 – 135.

(20) Curtarolo, S.; Hart, G. L. W.; Nardelli, M. B.; Sanvito, S.; Levy, O. The High-Throughput Highway to Computational Materials Design Recursively Stabilized Enumeration View Project Multi-Scale Modelling of Magnetic Tunnel Junctions View Project. *Nat. MATER.* **2013**, *12*, 191–201.

(21) Price, S. L. Why Don't We Find More Polymorphs? *Acta Crystallogr. Sect. B Struct. Sci. Cryst. Eng. Mater.* **2013**, *69*, 313–328.

(22) Saal, J. E.; Kirklin, S.; Aykol, M.; Meredig, B.; Wolverton, C. Materials Design and Discovery with High-Throughput Density Functional Theory: The Open Quantum Materials Database (OQMD). *JOM* **2013**, *65*, 1501–1509.

(23) Stevanović, V. Sampling Polymorphs of Ionic Solids Using Random Superlattices. *Phys. Rev. Lett.* **2016**, *116*, 075503.

(24) Sun, W.; Dacek, S. T.; Ong, S. P.; Hautier, G.; Jain, A.; Richards, W. D.; Gamst, A. C.; Persson, K. A.; Ceder, G. The Thermodynamic Scale of Inorganic Crystalline Metastability. *Sci. Adv.* **2016**, *2*, e1600225.

(25) Stein, A.; Keller, S. W.; Mallouk, T. E. Turning down the Heat: Design and Mechanism in Solid-State Synthesis. *Science.* **1993**, *259* (5101), 1558–1564.

(26) Aykol, M.; Dwaraknath, S. S.; Sun, W.; Persson, K. A. Thermodynamic Limit for Synthesis of Metastable Inorganic Materials. *Sci. Adv.* **2018**, *4*, eaaq0148.

(27) U. Schubert and N. Hüsing. *Synthesis of Inorganic Materials*, 3rd ed.; Wiley-VCH, 2012.

(28) Cruz-Cabeza, A. J.; Reutzel-Edens, S. M.; Bernstein, J. Facts and Fictions about Polymorphism . *Chem. Soc. Rev* **2015**, *44*, 8619–8635.

(29) Jones, E. B. and Stevanović, V. Polymorphism in Elemental Silicon: Probabilistic Interpretation of the Realizability of Metastable Structures. *Phys. Rev. B* **2017**, *96*, 184101.

(30) Parija, A.; Waetzig, G. R.; Andrews, J. L. and Banerjee, S. Traversing Energy Landscapes Away from Equilibrium: Strategies for Accessing and Utilizing Metastable Phase Space. *J. Phys. Chem. C.* **2018**, *122*, 25709–25728.

(31) van den Berg, A. J.; Juffermans, C. A. H. The Polymorphism of Silver Tungstate Ag_2WO_4. *J. Appl. Crystallogr.* **1982**, *15*, 114–116.

(32) Lin, Z.; Li, J.; Zheng, Z.; Yan, J.; Liu, P.; Wang, C.; Yang, G. Electronic Reconstruction of α-Ag_2WO_4 Nanorods for Visible-Light Photocatalysis. *ACS Nano.* **2015**, *9*, 7256–7265.

(33) Chávez, N. L. H.; de Avila, E. D.; Barbugli, P. A.; Oliveira, R. C.; Foggi, C. C.; Longo, E.; and Vergani, C. E. Promising Effects of Silver Tungstate Microcrystals on Fibroblast Human Cells and Three Dimensional Collagen Matrix Models: A Novel Non-Cytotoxic Material to Fight Oral Disease. *Colloids Surf. B* **2018**, *170*, 505–513.

(34) Roca, R. A.; Sczancoski, J. C.; Nogueira, I. C.; Fabbro, M. T.; Alves, H. C.; Gracia, L.; Santos, L. P. S.; De Sousa, C. P.; Andrés, J.; Luz, G. E.; Longo, E.; Cavalcante, L. S. Facet-Dependent Photocatalytic and Antibacterial Properties of α-Ag_2WO_4 Crystals: Combining Experimental Data and Theoretical Insights. *Catal. Sci. Technol* **2015**, *20*, 40–91.

(35) Tang, J.; Ye, J. Correlation of Crystal Structures and Electronic Structures and Photocatalytic Properties of the W-Containing Oxides. *J. Mater. Chem* **2005**, *15*, 4246–4251.

(36) Suthanthiraraj, S. A.; Sarajini, S. Ionic Transport and Surface Morphological Studies on SbI_3-Ag_2WO_4 Mixed System for Solid State Battery Applications. *Chem. Sci. Trans.* **2012**, *1*, 13–22.

(37) Cavalcante, L. S.; Almeida, P. M. A.; Avansi Jr., W; Tranquilin, R. L.; Longo, E.; Batista, N. C.; Mastelaro, V. R.; Siu Li, M. Cluster Coordination and Photoluminescence Properties of α-Ag_2WO_4 Microcrystals. *Inorg. Chem* **2012**, *51*, 10675–10687.

(38) Zhang, R.; Cui, H.; Yang, X.; Tang, H.; Liu, H.; Li, Y. Facile Hydrothermal Synthesis and Photocatalytic Activity of Rod-like Nanosized Silver Tungstate. *Micro Nano Lett.* **2012**, *7*, 1285–1288.

(39) da Silva, L. F.; Catto, A. C.; Avansi, W.; Ecio, L.; Cavalcante, S.; Andrés, J.; Andrés, A.; Aguir, K.; Mastelaro, V. R.; Longo, E. A Novel Ozone Gas Sensor Based on One-Dimensional (1D) a-Ag_2WO_4 Nanostructures. *Nanoscale* **2014**, *6*, 4058–4062.

(40) Longo, V. M.; De Foggi, C. C.; Ferrer, M. M.; Gouveia, A. F.; André, R. S.; Avansi, W.; Vergani, C. E.; Machado, A. L.; Andrés, J.; Cavalcante, L. S.; Hernandes, A. C.; Longo, E. Potentiated Electron Transference in α-Ag_2WO_4 Microcrystals with Ag Nanofilaments as Microbial Agent. *J. Phys. Chem. A* **2014**, *118*, 5769–5778.

(41) Dutta, D. P.; Singh, A.; Ballal, A.; Tyagi, A. K. High Adsorption Capacity for Cationic Dye Removal and Antibacterial Properties of Sonochemically Synthesized Ag_2WO_4 Nanorods. *Eur. J. Inorg. Chem.* **2014**, *2014*, 5724–5732.

(42) Longo, E.; P. Volanti, D.; M. Longo, V.; Gracia, L.; C. Nogueira, I.; A. P. Almeida, M.; N. Pinheiro, A.; M. Ferrer, M.; S. Cavalcante, L.; Andrés, J. Toward an Understanding of the Growth of Ag Filaments on α-Ag_2WO_4 and Their Photoluminescent Properties: A Combined Experimental and Theoretical Study. *J. Phys. Chem. C* **2014**, *118* (2), 1229–1239.

(43) Chen, H.; Xu, Y. Photoactivity and Stability of Ag_2WO_4 for Organic Degradation in Aqueous Suspensions. *Appl. Surf. Sci.* **2014**, *319*, 319–323.

(44) da Silva, L. F.; Catto, A. C.; Avansi Jr., W.; Cavalcante, L. S.; Mastelaro, V. R.; Andrés, J.; Aguir, K.; and Longo, E. Acetone Gas Sensor Based on α-Ag_2WO_4 Nanorods Obtained via a Microwave-Assisted Hydrothermal Route. *J. Alloy. Compd.* **2016**, *683*, 186–190.

(45) de Santana, Y. V. B.; Gomes, J. E. C.; Matos, L.; Cruvinel, G. H.; Perrin, A.; Perrin, C.; Andrès, J.; Varela, J. A.; and Longo, E. Silver Molybdate and Silver Tungstate Nanocomposites with Enhanced Photoluminescence. *Nanomater Nanotechnol.* **2014**, *4*, 10.5772/58923.

(46) Pinatti, I. M.; Nogueira, I. C.; Pereira, W. S.; Pereira, P. F. S.; Gonçalves, R. F.; Varela, J. A.; Longo, E.; Rosa, I. L. V. Structural and Photoluminescence Properties of Eu(3+) Doped α-Ag_2WO_4 Synthesized by the Green Coprecipitation Methodology. *Dalt. Trans.* **2015**, *44*, 17673–17685.

(47) Selvamani, M.; Krishnamoorthy, G.; Ramadossa, M.; Sivakumar, P. K.; Settu, M.; Ranganathan, S. . and V. N. Ag@$Ag_8W_4O_{16}$ Nanoroasted Rice Beads with Photocatalytic, Antibacterial and Anticancer Activity. *Mater. Sci. Eng. C.* **2015**, *60*, 109–118.

(48) de Foggi, Camila C.; de Oliveira, Regiane; Fabbro, Maria T.; Vergani, C. E. .; Andres, Juan; Longo, E.; L. Machado, A. Tuning the Morphological, Optical, and Antimicrobial Properties of α-Ag_2WO_4 Microcrystals Using Different Solvents. *Cryst. Growth Des.* **2017**, *17*, 6239–6246.

(49) Santos, C. J.; Filho, F. M.; Campos, F. L.; Ferreira, C. A.; de Barros, A. L. B.; and Soares, D. C. F. Ag_2WO_4 Nanoparticles Radiolabeled with Technetium-99m: A Potential New Tool for Tumor Identification and Uptake. *J Radioanal Nucl Chem.* **2020**, *323*, 51–59.

(50) George, T.; Joseph, S.; Mathew, S. Synthesis and Characterization of Nanophased Silver Tungstate. *Pramana-J. Phys.* **2005**, *65*, 793–799.

(51) Ng, C. H. B.; Fan, W. Y. Preparation of Highly Uniform 1-Dimensional α-Ag_2WO_4 Nanostructures with Controllable Aspect Ratio and Study of the Growth Mechanism. *CrystEngComm* **2016**, *18*, 8010–8019.

(52) Gupta, S. K.; Sudarshan, K.; Ghosh, P. S.; Mukherjee, S.; Kadam, R. M. Doping-Induced Room Temperature Stabilization of Metastable β-Ag_2WO_4 and Origin of Visible Emission in α-and β-Ag_2WO_4 : Low Temperature Photoluminescence Studies. *J. Phys. Chem. C* **2016**, *120*, 7265–7276.

(53) Macedo, N. G.; Gouveia, A. F.; Roca, R. A.; Assis, M. de; Gracia, L.; Andrés, J.; Leite, E. R.; Longo, E. Surfactant-Mediated Morphology and Photocatalytic Activity of α-Ag_2WO_4 Material. *J. Phys. Chem. C* **2018**, *122*, 8667–8679.

(54) Liu, D.; Huang, W.; Li, L.; Liu, L.; Sun, X.; Liu, B.; Yang, B.; Guo, C. Experimental and Theoretical Investigation on Photocatalytic Activities of 1D Ag/Ag_2WO_4 Nanostructures. *Nanotechnology.* **2017**, *28*, 385702.

(55) Hu, B.; Wu, L.-H.; Liu, S.-J.; Yao, H.-B.; Shi, H.-Y.; Li, G.-P.; Yu, S.-H. Microwave-Assisted Synthesis of Silver Indium Tungsten Oxide Mesocrystals and Their Selective Photocatalytic Propertiesw. *Chem. Commun.* **2010**, *46*, 2277–2279.

(56) Wang, X.; Fu, C.; Wang, P.; Yu, H.; Yu, J. Hierarchically Porous Metastable β-Ag_2WO_4 Hollow Nanospheres: Controlled Synthesis and High Photocatalytic Activity. *Nanotechnology.* **2013**, *24*, 165602.

(57) Laier, L. O.; Assis, M.; Foggi, C. C.; Gouveia, A. F.; Vergani, C. E.; Santana, L. C. L.; Cavalcante, L. S.; Andrés J.; and Longo, E. Surface-Dependent Properties of α-Ag_2WO_4: A Joint Experimental and Theoretical Investigation. *Theor Chem Acc.* **2020**, *139*,

108.

(58) Nobre, F. X.; Bastos, I. S.; dos Santos, R. O.; Araújo Jr, Edgar Alves; Takeno, Mitsuo Lopes; Manzato, Lizandro; de Matos, José Milton Elias; Orlandi, Patrícia Puccinelli; Mendes, Josilayne de Fátima Souza; Brito, Walter Ricardo; Couceiro, P. R. Antimicrobial Properties of α-Ag_2WO_4 Rod-like Microcrystals Synthesized by Sonochemistry and Sonochemistry Followed by Hydrothermal Conventional Method. *Ultrason. Sonochem.* **2019**, *58*, 104620.

(59) Ajabshir, S. Z.; Baladi, M.; Amiri, O. and Niasari, M. S. Sonochemical Synthesis and Characterization of Silver Tungstate Nanostructures as Visible-Light-Driven Photocatalyst for Waste-Water Treatment. *Sep. Purif. Technol.* **2020**, *248*, 117062.

(60) Wang, B.-Y.; Zhang, G.-Y.; Cui, G.-W.; Xu, Y.-Y.; Liu, Y.; Xing, C.-Y. Controllable Fabrication of α-Ag_2WO_4 Nanorod-Clusters with Superior Simulated Sunlight Photocatalytic Performance. *Inorg. Chem. Front.* **2019**, *6*, 209–219.

(61) Li, J.; Yu, C.; Zheng, C.; Etogo, A.; Xie, Y.; Zhong, Y.; Hu, Y. Facile Formation of Ag_2WO_4/AgX (X=Cl, Br, I) Hybrid Nanorods with Enhanced Visible-Light-Driven Photoelectrochemical Properties. *Mater. Res. Bull.* **2015**, *61*, 315–320.

(62) Zhang, X.-Y.; Wang, J.-D.; Liu, J.-K.; Yang, X.-H.; Lu, Y. Construction of Silver Tungstate Multilevel Sphere Clusters by Controlling the Energy Distribution on the Crystal Surface. *CrystEngComm.* **2015**, *17*, 1129–1138.

(63) Lemos, P. S.; Altomare, A.; Gouveia, A. F.; Nogueira, I. C.; Gracia, L.; Llusar, R.; Andrés, J.; Longo, E.; Cavalcante, L. S. Synthesis and Characterization of Metastable β-Ag_2WO_4: An Experimental and Theoretical Approach. *Dalt. Trans.* **2015**, *45*, 1185.

(64) Roca, R. A.; Lemos, P. S.; Andrés, J.; E. Longo, E. Formation of Ag Nanoparticles on Metastable β-Ag_2WO_4 Microcrystals Induced by Electron Irradiation. *Chem. Phys. Lett.*

2016, *644*, 68–72.

(65) Kumar Gupta, S.; Sudarshan, K.; Sarathi Ghosh, P.; Mukherjee, S.; Mahadeo Kadam, R. Doping-Induced Room Temperature Stabilization of Metastable β-Ag_2WO_4 and Origin of Visible Emission in α- and β-Ag_2WO_4: Low Temperature Photoluminescence Studies. *J. Phys. Chem. C* **2016**, *120*, 7265–7276.

(66) Roca, R. A.; Lemos, P. S.; Gracia, L.; Andrés, J.; Longo, E. Uncovering the Metastable γ-Ag_2WO_4 Phase: A Joint Experimental and Theoretical Study. *RSC Adv.* **2017**, *7*, 5610–5620.

(67) Neto, N. F. A.; Silva, J. M. P.; Tranquilin, R. L.; Longo, E.; Bomio, M. R. D.; and Motta, F. V. Stabilization of the γ-Ag_2WO_4 Metastable Pure Phase by Coprecipitation Method Using Polyvinylpyrrolidone as Surfactant: Photocatalytic Property. *Ceram. Int.* **2020**, *46*, 14864–14871.

(68) Roca, R. A.; Gouveia, A. F.; Lemos, P. S.; Gracia, L.; Andre, J.; Longo, E. Formation of Ag Nanoparticles on β-Ag_2WO_4 through Electron Beam Irradiation: A Synergetic Computational and Experimental Study. *Inorg. Chem.* **2016**, *55*, 8661–8671.

(69) Michalowicz, A.; Moscovici, J.; Muller-Bouvet, D.; and Provost, K. MAX: Multiplatform Applications for XAFS. *J. Phys. Conf. Ser.* **2009**, *190*, 012034.

(70) De Foggi, C. C. ; De Oliveira, R. C.; Assis, M.; Fabbro, M. T.; Mastelaro, V. R.; Vergani, C. E.; Gracia, L.; Andrés, J.; Longo, E.; Machado, A. L. Unvealing the Role of β-Ag_2MoO_4 Microcrystals to the Improvement of Antibacterial Activity. *Mater. Sci. Eng. C.* **2020**, *111*, 110765.

(71) Perdew, J. P.; Chevary, J. A.; Vosko, S. H.; Jackson, K. A.; Pederson, M. R.; Singh, D. J.; and Fiolhais, C. Atoms, Molecules, Solids, and Surfaces: Applications of the Generalized Gradient Approximation for Exchange and Correlation. *Phys. Rev. B.* **1992**,

46, 6671.

(72) Perdew, J. P.; Burke K.; Ernzerhof, M. Generalized Gradient Approximation Made Simple. *Phys. Rev. Lett.* **1996**, *77*, 3865–3868.

(73) Kresse, G.; and Furthmüller, J. Efficient Iterative Schemes for Ab Initio Total-Energy Calculations Using a Plane-Wave Basis Set. *Phys. Rev. B.* **1996**, *54*, 11169.

(74) Kresse, G.; and Furthmüller, J. Efficiency of Ab-Initio Total Energy Calculations for Metals and Semiconductors Using a Plane-Wave Basis Set. *Comput. Mater. Sci.* **1996**, *6*, 15–50.

(75) Momma, K.; and Izumi, F. VESTA 3 for Three-Dimensional Visualization of Crystal, Volumetric and Morphology Data. *J. Appl. Crystallogr.* **2011**, *44*, 1272–1276.

(76) Barmparis, G. D.; Lodziana, Z.; Lopez, N.; Remediakis, I. N. Nanoparticle Shapes by Using Wulff Constructions and First-Principles Calculations. *Beilstein J. Nanotechnol.* **2015**, *6*, 361–368.

(77) Andrés, J.; Gracia, L.; Gouveia, A. F.; Ferrer, M. M.; and Longo, E. Effects of Surface Stability on the Morphological Transformation of Metals and Metal Oxides as Investigated by First-Principles Calculations. *Nanotechnology.* **2015**, *26*, 405703.

(78) Byzynski, G.; Melo, C.; Volanti, D. P.; Ferrer, M. M.; Gouveia, A. F.; Ribeiro, C.; Andrés, J.; Longo, E. The Interplay between Morphology and Photocatalytic Activity in ZnO and N-Doped ZnO Crystals. *Mater. Des.* **2017**, *120*, 363–375.

(79) Ribeiro, R. A. P.; Oliveira, M. C.; Bomio, M. R. D.; de Lazaro, S. R.; Andrés, J.; Longo, E. Connecting the Surface Structure, Morphology and Photocatalytic Activity of Ag_2O: An in Depth and Unified Theoretical Investigation. *Appl. Surf. Sci.* **2020**, *509*,

(80) Botelho, G.; Andres, J.; Gracia, L.; Matos, L. S.; Longo, E. Photoluminescence and Photocatalytic Properties of Ag_3PO_4 Microcrystals: An Experimental and Theoretical

Investigation. *Chempluschem.* **2016**, *81*, 202–212.

(81) Trench, A. B.; Machado, T. R.; Gouveia, A. F.; Assis, M.; da Trindade, L. G.; Santos, C.; Perrin, A.; Perrin, C.; Oliva, M.; Andrés, J.; Longo, E. Connecting Structural, Optical, and Electronic Properties and Photocatalytic Activity of Ag_3PO_4:Mo Complemented by DFT Calculations. *Appl. Catal. B Environ.* **2018**, *238*, 198–211.

(82) Bomio, M. R. D.; Tranquilin, R. L.; Motta, F. V.; Paskocimas, C. A.; Nascimento, R. M.; Gracia, L.; Andres, J.; Longo, E. Toward Understanding the Photocatalytic Activity of $PbMoO_4$ Powders with Predominant (111), (100), (011), and (110) Facets. A Combined Experimental and Theoretical Study. *J. Phys. Chem. C.* **2013**, *117*, 21382–21395.

(83) Oliveira, M. C.; Gracia, L.; Nogueira, I. C.; Do Carmo Gurgel, M. F.; Mercury, J. M. R.; Longo, E.; Andrés, J. Synthesis and Morphological Transformation of $BaWO_4$ Crystals: Experimental and Theoretical Insights. *Ceram. Int.* **2016**, *42*, 10913–10921.

(84) Gouveia, A. F.; Assis, M.; Cavalcante, L. S.; Gracia, L.; Longo, E.; Andrés, J. Reading at Exposed Surfaces: Theoretical Insights into Photocatalytic Activity of $ZnWO_4$. *Front. Res. Today.* **2018**, *1*, 1005.

(85) Pereira, P. F. S.; Gouveia, A. F.; Assis, M.; Oliveira, R. C. De; Pinatti, I. M.; Penha, M.; Gracia, L.; Andre, J.; Longo, E. $ZnWO_4$ Nanocrystals: Synthesis, Morphology, Photoluminescence and Photocatalytic Properties. *Phys. Chem. Chem. Phys.* **2018**, *20*, 1923–1937.

(86) Andrés, J.; Gracia, L.; Gouveia, A. F.; Ferrer, M. M.; Longo, E. Effects of Surface Stability on the Morphological Transformation of Metals and Metal Oxides as Investigated by First-Principles Calculations. *Nanotechnology.* **2015**, *26*, 405703.

(87) Ferrer, M. M.; Gouveia, A. F.; Gracia, L.; Longo, E.; and Andrés, J. A 3D Platform for the Morphology Modulation of Materials: First Principles Calculations on the

Thermodynamic Stability and Surface Structure of Metal Oxides: Co_3O_4, α-Fe_2O_3, and In_2O_3. *Model. Simul. Mater. Sci. Eng.* **2016**, *24*, 025007.

(88) Gouveia, A. F.; Ferrer, M. M.; Sambrano, J. R.; Andrés, J.; Longo, E. Modeling the Atomic-Scale Structure , Stability , and Morphological Transformations in the Tetragonal Phase of $LaVO_4$. *Chem. Phys. Lett.* **2016**, *660*, 87–92.

(89) Dura, O. J.; Boada, R.; López de la Torre, M. A.; Aquilanti, G.; Rivera-Calzada, A.; Leon, C. . and C. J. XANES and EXAFS Study of the Local Order in Nanocrystalline Yttria-Stabilized Zirconia. *Phys. Rev. B.* **2013**, *87*, 174109.

(90) Catto, A. C.; Fiorido, T.; Souza, E. L. S.; Avansi Jr., W.; Andres, J.; Aguir, K.; Longo, E.; Cavalcante, L. S.; da Silva, L. F. Improving the Ozone Gas-Sensing Properties of $CuWO_4$ Nanoparticles. *J. Alloys Compd.* **2018**, *748*, 411–417.

(91) Yamazoe, S.; Hitomi, Y.; Shishido, T.; Tanaka, T. XAFS Study of Tungsten L 1- and L 3-Edges: Structural Analysis of WO_3 Species Loaded on TiO_2 as a Catalyst for Photo-Oxidation of NH_3. *J. Phys. Chem. C* **2008**, *112*, 6869–6879.

(92) Kuzmin, A.; and Purans, J. Local Atomic and Electronic Structure of Tungsten Ions in AWO_4 Crystals of Scheelite and Wolframite Types. *Radiat. Meas.* **2001**, *33*, 583–586.

(93) Poirier, G.; Cassanjes, F.; Messaddeq, Y.; Ribeiro, S.; Michalowicz, A.; and Poulain, M. Local Order around Tungsten Atoms in Tungstate Fluorophosphate Glasses by X-Ray Absorption Spectroscopy. *J. Non. Cryst. Solids.* **2005**, *351*, 3644–3648.

(94) da Silva, G. T. S. T.; Carvalho, K. T. G.; Lopes, O. F.; Ribeiro, C. g-C_3N_4/Nb_2O_5 Heterostructures Tailored by Sonochemical Synthesis: Enhanced Photocatalytic Performance in Oxidation of Emerging Pollutants Driven by Visible Radiation. *Appl. Catal. B Environ.* **2017**, *216*, 70–79.

(95) Lopes, O. F.; Carvalho, K. T. G.; Avansi, W.; Milori, D. M. B.; Ribeiro, C. Insights

into the Photocatalytic Performance of $Bi_2O_2CO_3/BiVO_4$ Heterostructures Prepared by One-Step Hydrothermal Method. *RSC Adv.* **2018**, *8*, 10889–10897.

(96) Macedo, N. G.; Machado, T. R.; Roca, R. A.; Assis, M.; Foggi, C. C.; Puerto-Belda, V.; Mínguez-Vega, G.; Rodrigues, A.; San-Miguel, M. A.; Cordoncillo, E.; Beltrán-Mir, H.; Andrés, J.; Longo, E. Tailoring the Bactericidal Activity of Ag Nanoparticles/α-Ag_2WO_4 Composite Induced by Electron Beam and Femtosecond Laser Irradiation: Integration of Experiment and Computational Modeling. *ACS Appl. Bio Mater.* **2019**, *2*, 824–837.

(97) Yi, H.; Yan, M.; Huang, D.; Zeng, G.; Lai, C.; Li, M.; Huo, X.; Qin, L., Liu, S.; Liu, X.; Li, B.; Wang, H.; Shen, M.; Fu, Y.; Guo, X. Synergistic Effect of Artificial Enzyme and 2D Nano-Structured Bi_2WO_6 for Eco-Friendly and Efficient Biomimetic Photocatalysis. *Appl. Catal. B Environ.* **2019**, *250*, 52–62.

(98) Huo, X.; Yang, Y.; Niu, Q.; Zhu, Y.; Zeng, G.; Lai, C.; Yi, H.; Li, M.; An, Z.; Huang, D.; Fu, Y.; Li, B.; Li, L.; Zhang, M. A Direct Z-Scheme Oxygen Vacant BWO/Oxygen-Enriched Graphitic Carbon Nitride Polymer Heterojunction with Enhanced Photocatalytic Activity. *Chem. Eng. J.* **2021**, *403*, 126363.

(99) Sivakumar, R.; Gopalakrishnan, R.; Jayachandran, M.; and Sanjeeviraja, C. Investigation of X-Ray Photoelectron Spectroscopic (XPS), Cyclic Voltammetric Analyses of WO_3 Films and Their Electrochromic Response in FTO/WO_3/Electrolyte/FTO Cells. *Smart Mater. Struct.* **2006**, *15*, 877–888.

(100) Liu, H.; Yang, W.; Ma, Y.; Cao, Y.; Yao, J.; Zhang, J.; and Hu, T. Synthesis and Characterization of Titania Prepared by Using a Photoassisted Sol−Gel Method. *Langmuir.* **2003**, *19*, 3001–3005.

(101) Kruse, N. . and S. C. XPS Characterization of Au/TiO_2 Catalysts: Binding Energy

Assessment and Irradiation Effects. *Appl. Catal.* **2011**, *391*, 367–376.

(102) Yan, Y.; Yang, H.; Zhao, X.; Li, R. . and W. Enhanced Photocatalytic Activity of Surface Disorder-Engineered $CaTiO_3$. *Mater Res Bull.* **2018**, *105*, 286–290.

(103) Gligorovski, S.; Strekowski, R.; Barbati, S.; and Vione, V. Environmental Implications of Hydroxyl Radicals (•OH). *Chem. Rev.* **2015**, *115*, 13051–13092.

(104) Nosaka, Y.; and Nosaka, A. Understanding Hydroxyl Radical (•OH) Generation Processes in Photocatalysis. *ACS Energy Lett.* **2016**, *1*, 356–359.

(105) Chen, D.; He, D.; Lu, J.; Zhong, L.; Liu, F.; Liu, J.; Yu, J.; Wan, G.; He, S.; and Luo, Y. Investigation of the Role of Surface Lattice Oxygen and Bulk Lattice Oxygen Migration of Cerium-Based Oxygen Carriers: XPS and Designed H_2-TPR Characterization. *Appl. Catal. B-Environ.* **2017**, *218*, 249–259.

(106) Zhao, J.; Liu, C.; Li, J.; Wu, R.; Wang, J.; Qian, H.; Guo, H.; Li, J.; and Ibrahim, K. Oxygen Vacancy Induced Electronic Structure Variation in the $La_{0.2}Sr_{0.8}MnO_3$ Thin Film. *AIP Adv.* **2019**, *9*, 055208.

(107) Shao, M.; Liu, J.; Ding, W.; Wang, J.; Dong, F. . and Z. Oxygen Vacancy Engineering of Self-Doped SnO_{2-x} Nanocrystals for Ultrasensitive NO_2 Detection. *J. Mater. Chem. C.* **2020**, *8*, 487–494.

(108) Botelho, G.; Sczancoski, J. C.; Andres, J.; Gracia, L.; Longo, E. Experimental and Theoretical Study on the Structure, Optical Properties, and Growth of Metallic Silver Nanostructures in Ag_3PO_4. *J. Phys. Chem. C* **2015**, *119*, 6293–6306.

(109) Fabbro, M. T.; Gracia, L.; Silva, G. S.; Santos, L. P. S.; Andrés, J.; Cordoncillo, E.; Longo, E. Understanding the Formation and Growth of Ag Nanoparticles on Silver Chromate Induced by Electron Irradiation in Electron Microscope: A Combined Experimental and Theoretical Study. *J. Solid State Chem.* **2016**, *239*, 220–227.

(110) de Oliveira, R. C.; Assis, M.; Teixeira, M. M.; da Silva, M. D. P.; Li, M. S.; Andres, J.; Gracia, L.; Longo, E. An Experimental and Computational Study of β-$AgVO_3$: Optical Properties and Formation of Ag Nanoparticles. *J. Phys. Chem. C* **2016**, *120*, 12254–12264.

(111) Lemos, P. S.; Silva, G. S.; Roca, R. A.; Assis, M.; Torres-Mendieta, R.; Beltrán-Mir, H.; Mínguez-Vega, G.; Cordoncillo, E.; Andrés, J.; Longo, E. . Laser and Electron Beam-Induced Formation of Ag/Cr Structures on Ag_2CrO_4. *Phys. Chem. Chem. Phys.* **2019**, *21*, 6101–6111.

(112) Andrés, J.; Gouveia, A. F.; Gracia, L.; Longo, E.; Manzeppi Faccin, G; da Silva, E. Z.; Pereira, D. H.; San-Miguel, M. A. Formation of Ag Nanoparticles under Electron Beam Irradiation: Atomistic Origins from First-Principles Calculations. *Int. J. Quantum Chem.* **2018**, *118*, e25551.

(113) Pereira, W. da S.; Andrés, J.; Gracia, L.; San-Miguel, M. A.; da Silva, E. Z.; Longo, E.; and Longo, V. M. Elucidating the Real-Time Ag Nanoparticle Growth on α-Ag_2WO_4 during Electron Beam Irradiation: Experimental Evidence and Theoretical Insights. *Phys. Chem. Chem. Phys.* **2015**, *17*, 5352–5359.

(114) Vatansever, F.; de Melo, W. C. M. A.; Avci, P.; Vecchio, D.; Sadasivam, M.; Gupta, A.; Chandran, R.; Karimi, M.; Parizotto, N. A.; Yin, R.;Tegos, V. . and H. Antimicrobial Strategies Centered around Reactive Oxygen Species - Bactericidal Antibiotics, Photodynamic Therapy and Beyond. *FEMS Microbiol. Rev.* **2013**, *37*, 955–989.

(115) de Foggi, C. C.; de Oliveira, R. C.; Fabbro, M. T.; Vergani, C. E.; Andres, J.; Longo, E.; and Machado, A. L. Tuning the Morphological, Optical, and Antimicrobial Properties of α-Ag_2WO_4 Microcrystals Using Different Solvents. *Cryst. Growth Des.* **2017**, *17*, 6239–6246.

(116) Li, Q.; Mahendra, S.; Lyon, D. Y.; Brunet, L.; Liga, M. V.; Li, D.; and Alvarez, P. J. J. Antimicrobial Nanomaterials for Water Disinfection and Microbial Control: Potential Applications and Implications. *Water Res.* **2008**, *42*, 4591–4602.

(117) Qi, K.; Xing, X.; Zada, A.; Li, M.; Wang, Q.; Liu, S.; Lin, H. . and G. W. Transition Metal Doped ZnO Nanoparticles with Enhanced Photocatalytic and Antibacterial Performances: Experimental and DFT Studies. *Ceram. Inter.* **2020**, *46*, 1494–1502.

(118) Kröger, F. A.; and Vink, H. J. Relations between the Concentrations of Imperfections in Crystalline Solids. *Solid State Phys.* **1956**, *3*, 307–435.

(119) Gebauer, D.; Kellermeier, M.; Gale, J. D.; Bergström, L.; Cölfen, H. Pre-Nucleation Clusters as Solute Precursors in Crystallisation. *Chem. Soc. Rev.* **2014**, *43*, 2348–2371.

(120) Zahn, D. Thermodynamics and Kinetics of Prenucleation Clusters, Classical and Non-Classical Nucleation. *ChemPhysChem.* **2015**, *16*, 2069–2075.

(121) Demichelis, R.; Raiteri, P.; Gale, J. D.; Quigley, D. . G. Stable Prenucleation Mineral Clusters Are Liquid-like Ionic Polymers. *Nat. Commun.* **2011**, *2*, 590.

For Table of Contents Only

This study presents the selective-controlled synthesis of α, β, and γ-Ag_2WO_4 polymorphs and offers new insights regarding the various parameters that command the physico-chemical behavior of the Ag_2WO_4 polymorphs. The experimental and theoretical results allow us to rationalize a structure–property relationship among the morphology, and photocatalytic and antibacterial activities.